We greatly value the careful reading and the detailed comments provided by the referees. The responses to the comments of referee 1 in our direct reply (shown below) and within the revised manuscript (see marked copy) are provided. The pages and lines indicated below correspond to those in the marked copy.

Response to Referee 1 (Referees' comments are italicized)

1. Referee comment: "*The authors have well addressed my comments for an earlier version of manuscript except for the one on pH definition. The revised manuscript says that "rH+ is the molarity-based hydronium ion activity coefficient (assumed to be 1), Haq+ (mole L-1) is the molar concentration of hydronium ions in particle water (i.e., pH is calculated in terms of molarity)". My understanding is that the molarity (or molar concentration) is defined on the basis of volume of the solution instead of that of the water. Haq+ calculated by ISORROPIA is actually the molality (mole kg-1 water). Please correct me if I was wrong. See more here: https://en.wikipedia.org/wiki/Molar_concentration*"

Author response: The referee is correct, and we have changed the manuscript to state that it is molality-based:

Page 10 line 273: "Since most thermodynamic equilibrium models (e.g., ISORROPIA-II, E-AIM) do not report liquid concentrations, but instead report species in terms of concentration per volume of air (e.g., µg m^{-3}, µmol m^{-3}), we have calculated the particle pH by:

$$pH = -\log_{10} \gamma_{H^+} H^+_{aq} = -\log_{10} \frac{1000 \gamma_{H^+} H^+_{air}}{W_i + W_o} \cong -\log_{10} \frac{1000 \gamma_{H^+} H^+_{air}}{W_i} \quad \textbf{(1b)}$$

where γ_{H^+} is the hydronium ion activity coefficient (assumed to be 1), H^+_{aq} is the concentration of hydronium ions in particle water in mole L^{-1} (i.e., the density of water is assumed to be 1000 kg m^{-3}, and so pH is calculated in terms of molality), H^+_{air} (µg m^{-3}) is the hydronium ion concentration per volume of air, and W_i and W_o (µg m^{-3}) are the bulk particle water concentrations associated with inorganic and organic species per volume of air, respectively. In equation 1b, the molecular weight of H$^+$ is taken as 1 g mole^{-1}, and 1000 is the factor needed for unit conversion of g L^{-1} to µg m^{-3}. H^+_{air} and W_i are outputs of the ISORROPIA-II model."

The referee is correct in stating that H^+_{aq} has units of molality (mol kg^{-1}). However, H^+_{aq} is not reported by ISORROPIA but is defined in equation 1b. As stated in the manuscript, ISORROPIA report species in terms of concentration per volume of air (e.g., µg m^{-3}, µmol m^{-3}). H^+_{air} and W_i are outputs of the ISORROPIA model, and they are expressed in terms of µg m^{-3} by ISORROPIA. In using H^+_{air} and W_i in Equation 1b to calculate the aerosol pH, we are defining H^+_{aq} as a molality-based concentration.

We refer the referee to page 8 of the User's Manual found on the ISORROPIA website (http://isorropia.eas.gatech.edu/index.php?title=User%27s_Manual) for more information regarding the units used by ISORROPIA.

2. Referee comment: "*I have another minor comment on this change made in the revised manuscript: Page 25 line 791: "In addition, formic and acetic acids may not be internally mixed with most of the other PM1 aerosol components (e.g., SO42-, NO3-, NH4+, CH3CO2H), and thus are not associated with acidic aerosols, as assumed above." What does "CH3CO2H" mean here?*"

Author response: CH_3COOH is the chemical formula of acetic acid. We meant to write $C_2O_4^{2-}$, chemical formula of oxalate, which has been shown to be internally mixed with PM_1 aerosol components SO_4^{2-}, NO_3^-, NH_4^+ in section 3.5.1 of our manuscript. This is corrected in the revised manuscript:

Page 25 line 717: "In addition, formic and acetic acids may not be internally mixed with most of the other PM_1 aerosol components (e.g., SO_4^{2-}, NO_3^-, NH_4^+, $C_2O_4^{2-}$), and thus are not associated with acidic aerosols, as assumed above."

<u>Additional minor revisions</u>

1. The affiliation of the first author was updated.

2. We changed the range of the x-axis of graphs shown in Figs. 4, 7, 8, S12 and S13. The x-axis of the previous version of these graphs had their range starting from pH value -2. The x-axis of the revised version of these graphs have their range starting from pH value -1. We made these changes because the particle pH of ambient aerosol does not go below -1. Note that these changes do not affect our results.

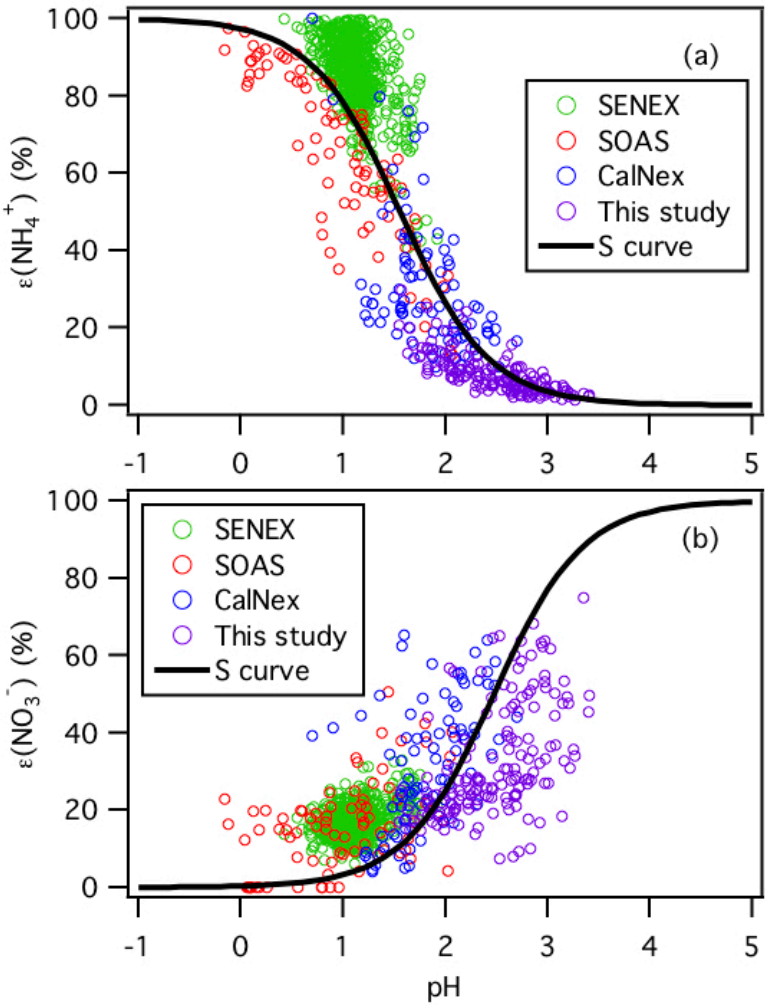

Figure 4: Analytically calculated S curves of $\varepsilon(NH_4^+)$ and $\varepsilon(NO_3^-)$ and ambient data plotted against ISORROPIA-predicted particle pH for this study, SENEX, SOAS and CalNex. For the ambient datasets, a narrow range of W_i (1 to 4 μg m^{-3}) and temperature (15 to 25 °C) are selected to be close to the analytical calculation input (i.e., W_i = 2.5 μg m^{-3} and temperature = 20 °C). Similar to Guo et al. (2017a), $\gamma_{NH_4^+} = 1$ and $\gamma_{H^+-NO_3^-} = \sqrt{\gamma_{H^+}\gamma_{NO_3^-}} = 0.28$ are used for the analytically calculated S curves.

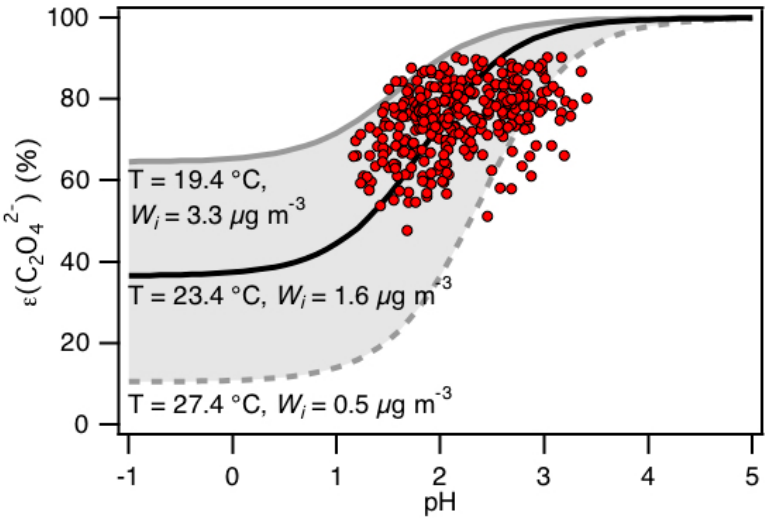

Figure 7: Analytically calculated S curve of $\varepsilon(C_2O_4^{2-})$ and ambient data from 13 September to 6 October 2016 plotted against ISORROPIA-predicted particle pH. For the ambient data, a range in W_i (0.5 to 4 μg m^{-3}) and temperature (15 to 31 °C) are chosen to be close to the analytically calculated outputs. For the analytically calculated S curves, we used $\gamma_{C_2H_2O_4}$ = 0.0492 (AIOMFAC predicted). We also assumed that $\gamma_{H^+}\gamma_{C_2HO_4^-} = \gamma_{H^+}\gamma_{NO_3^-}$, and used the ISORROPIA-predicted $\gamma_{H^+-NO_3^-} = \sqrt{\gamma_{H^+}\gamma_{NO_3^-}}$ = 0.265. The black line is the S curve calculated using the selected time period's average temperature (23.4 ± 4.0 °C) and W_i (1.6 ± 1.7 μg m^{-3}). The grey lines are S curves calculated using one standard deviation from the average temperature and W_i (i.e., temperature = 27.4 °C and W_i = 0.5 μg m^{-3} for dotted grey line, temperature = 19.4 °C and W_i = 3.3 μg m^{-3} for solid grey line).

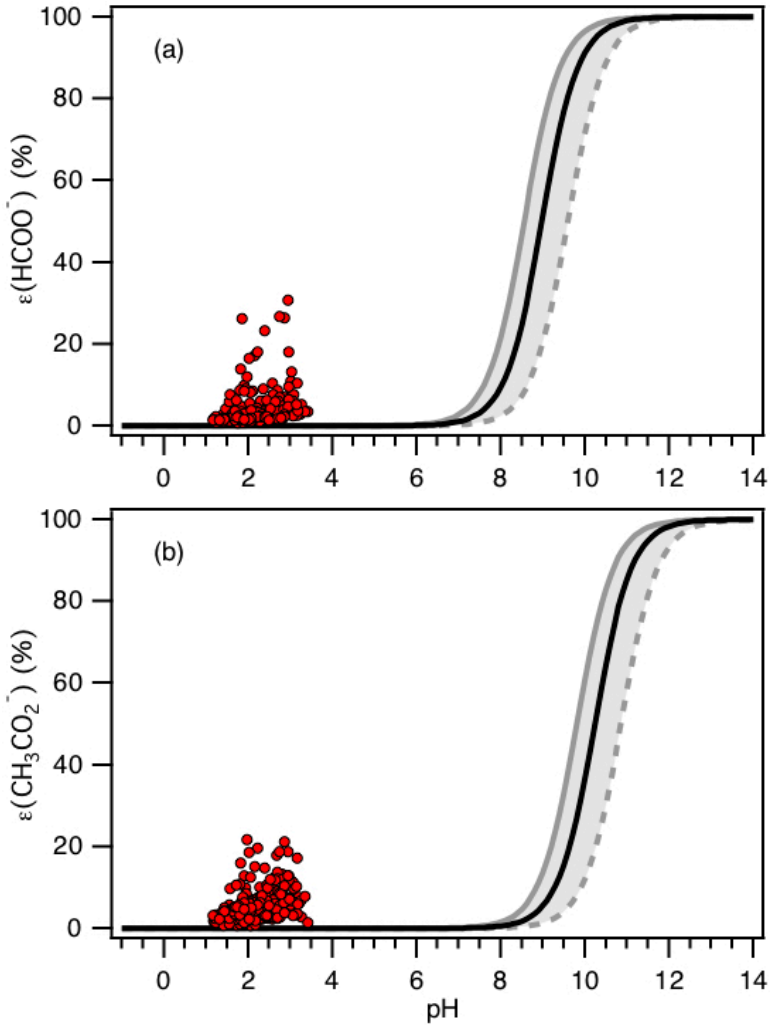

Figure 8: Analytically calculated S curves of $\varepsilon(HCOO^-)$ and $\varepsilon(CH_3CO_2^-)$ (solid black lines) and ambient data from 13 September to 6 October 2016 plotted against ISORROPIA-predicted particle pH (shown in panels (a) and (b), respectively). For the ambient data, a narrow range in W_i (0.5 to 4 μg m^{-3}) and RH (20 to 90 %) is chosen to be close to the analytically calculated outputs. For the analytically calculated S curves, we used γ_{HCOOH} = 0.334 and γ_{CH_3COOH} = 2.150 (AIOMFAC predicted). We also assumed that $\gamma_{H^+}\gamma_{HCOO^-} = \gamma_{H^+}\gamma_{CH_3COO^-} = \gamma_{H^+}\gamma_{NO_3^-}$, and used the ISORROPIA-predicted $\gamma_{H^+-NO_3^-} = \sqrt{\gamma_{H^+}\gamma_{NO_3^-}}$ = 0.265. The black lines are S curves calculated using the selected time period's average temperature (23.4 ± 4.0 °C) and W_i (1.6 ± 1.7 μg m^{-3}). The grey lines are S curves calculated using one standard deviation from the average temperature and W_i (i.e., temperature = 27.4 °C and W_i = 0.5 μg m^{-3} for dotted grey line, temperature = 19.4 °C and W_i = 3.3 μg m^{-3} for solid grey line).

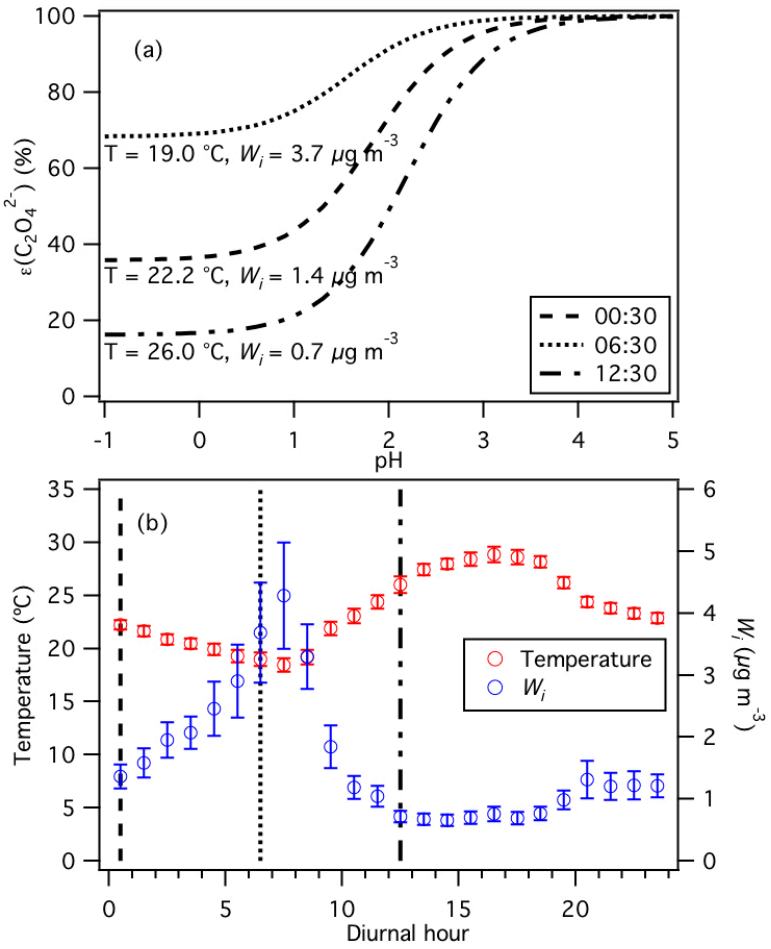

Figure S12: (a) Analytically calculated S curves of $\varepsilon(C_2O_4^{2-})$ at different times of the day: 00:30, 06:30 and 12:30. These S curves are calculated using values obtained from (b) the diurnal profiles of temperature and W_i. The set of 1-hour average temperatures and W_i at diurnal hours 00:30, 06:30 and 12:30 is used to calculate each S curve shown in panel (a). Similar to Fig. 7, we used $\gamma_{C_2H_2O_4}$ = 0.0492 (AIOMFAC predicted) and assumed that $\gamma_{H^+-NO_3^-} = \sqrt{\gamma_{H^+}\gamma_{NO_3^-}} = \sqrt{\gamma_{H^+}\gamma_{C_2HO_4^-}}$ = 0.265 (ISORROPIA-II predicted) to generate these S curves.

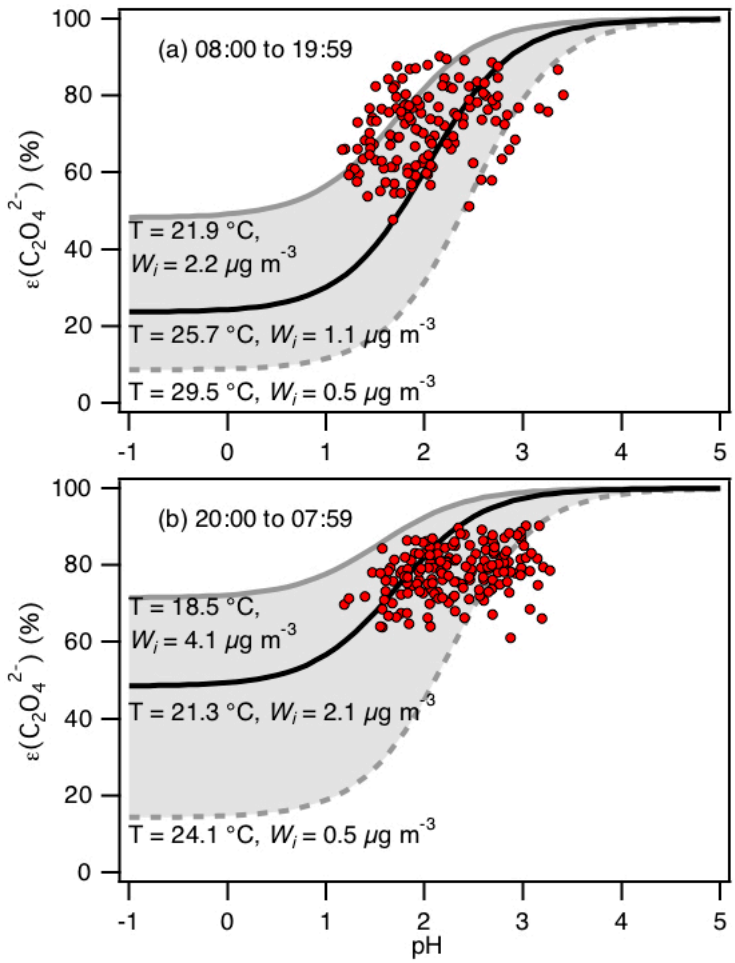

Figure S13: Analytically calculated S curve of ε($C_2O_4^{2-}$) and ambient data from 13 September to 6 October 2016 plotted against ISORROPIA-predicted particle pH. For the ambient data, a narrow range in W_i (0.5 to 4 μg m^{-3}) and RH (20 to 90 %) is chosen to be close to the analytically calculated outputs. We divided the ambient data into two sets: panel (a) 08:00 to 19:59, and panel (b) 20:00 to 07:59. For both analytically calculated S curves, we used $\gamma_{C_2H_2O_4}$ = 0.0492 (AIOMFAC predicted). We also assumed that $\gamma_{H^+}\gamma_{C_2HO_4^-} = \gamma_{H^+}\gamma_{NO_3^-}$, and used the ISORROPIA-predicted $\gamma_{H^+-NO_3^-} = \sqrt{\gamma_{H^+}\gamma_{NO_3^-}}$ = 0.265. In panel (a), we used the average temperature and W_i (25.7 ± 3.8 °C and 1.1 ± 1.1 μg m^{-3}) for the data between 08:00 to 19:59 to calculate the S curve (black line). In panel (b), we used the average temperature and W_i (21.3 ± 2.8 °C and 2.1 ± 2.0 μg m^{-3}) for the data between 20:00 to 07:59 to calculate the S curve (black line). Grey lines in both panels are S curves calculated using one standard deviation from the average temperature and W_i for the two datasets. In panel (a), the dotted grey line is the S curve calculated using 29.5 °C

and 0.5 μg m^{-3} while the solid grey line is the S curve calculated using 21.9 °C and 2.2 μg m^{-3}. In panel (b), the dotted grey line is the S curve calculated using 24.1 °C and 0.5 μg m^{-3} while the solid grey line is the S curve calculated using 18.5 °C and 4.1 μg m^{-3}.

Characterization of Aerosol Composition, Aerosol Acidity and Organic Acid Partitioning at an Agriculture-Intensive Rural Southeastern U.S. Site

Theodora Nah,[1,a] Hongyu Guo,[1] Amy P. Sullivan,[2] Yunle Chen,[1] David J. Tanner,[1] Athanasios Nenes,[1,3,4,5] Armistead Russell,[6] Nga Lee Ng,[1,3] L. Gregory Huey[1] and Rodney J. Weber[1,*]

[1]*School of Earth and Atmospheric Sciences, Georgia Institute of Technology, Atlanta, GA, USA*
[2]*Department of Atmospheric Science, Colorado State University, Fort Collins, CO, USA*
[3]*School of Chemical and Biomolecular Engineering, Georgia Institute of Technology, Atlanta, GA, USA*
[4]*ICE-HT, Foundation for Research and Technology, Hellas, 26504 Patras, Greece*
[5]*IERSD, National Observatory of Athens, P. Penteli, 15236, Athens, Greece*
[6]*School of Civil and Environmental Engineering, Georgia Institute of Technology, Atlanta, GA, USA*
[a]*Now at School of Energy and Environment, City University of Hong Kong, Kowloon, Hong Kong, China*

** To whom correspondence should be addressed: rweber@eas.gatech.edu*

Abstract

The implementation of stringent emission regulations has resulted in the decline of anthropogenic pollutants including sulfur dioxide (SO_2), nitrogen oxides (NO_x) and carbon monoxide (CO). In contrast, ammonia (NH_3) emissions are largely unregulated, with emissions projected to increase in the future. We present real-time aerosol and gas measurements from a field study conducted in an agricultural-intensive region in the southeastern U.S. during the fall of 2016 to investigate how NH_3 affects particle acidity and secondary organic aerosol (SOA) formation via the gas-particle partitioning of semi-volatile organic acids. Particle water and pH were determined using the ISORROPIA-II thermodynamic model and validated by comparing predicted inorganic HNO_3-NO_3^- and NH_3-NH_4^+ gas-particle partitioning ratios with measured values. Our results showed that despite the high NH_3 concentrations (average 8.1 ± 5.2 ppb), PM_1 were highly acidic with pH values ranging from 0.9 to 3.8, and an average pH of 2.2 ± 0.6. PM_1 pH varied by approximately 1.4 units diurnally. Formic and acetic acids were the most abundant gas-phase organic acids, and oxalate was the most abundant particle-phase water-soluble organic acid anion. Measured particle-phase water-soluble organic acids were on average 6 % of the total non-refractory PM_1 organic aerosol mass. The measured molar fraction of oxalic acid in the particle phase (i.e., particle-phase oxalic acid molar concentration divided by the total oxalic acid molar concentration) ranged between 47 and 90 % for PM_1 pH 1.2 to 3.4. The measured oxalic acid gas-particle partitioning ratios were in good agreement with their corresponding thermodynamic predictions, calculated based on oxalic acid's physicochemical properties, ambient temperature, particle water and pH. In contrast, gas-particle partitioning of formic and acetic acids were not well predicted for reasons

currently unknown. For this study, higher NH_3 concentrations relative to what has been measured in the region in previous studies had minor effects on PM_1 organic acids and their influence on the overall organic aerosol and PM_1 mass concentrations.

1. Introduction

Ammonia (NH_3) is the most abundant basic gas in the troposphere and plays an important role in many atmospheric processes. It is a major neutralizer of atmospheric acidic species, reacting readily with sulfuric acid (H_2SO_4) and nitric acid (HNO_3) to form ammonium sulfate and nitrate salts (e.g., $(NH_4)_2SO_4$, and other forms such as NH_4HSO_4, $(NH_4)_3H(SO_4)_2$, and NH_4NO_3), which are often the main inorganic components of atmospheric aerosols. The formation of particle-phase ammonium sulfate and nitrate salts in the aerosol phase depends on the thermodynamic states of their precursors and the environmental conditions, which can consequently affect aerosol pH. For example, Guo et al. (2017b) showed that for Southeast U.S. summertime conditions, as aerosol pH increases, the relative fractions of SO_4^{2-} and HSO_4^- increases and decreases, respectively. Wet and dry deposition are the principle NH_3 sinks (Dentener and Crutzen, 1994). NH_3 is spatially heterogeneous, with the highest concentrations typically found near emission sources (Seinfeld and Pandis, 2016). The dominant NH_3 sources in rural areas are agricultural in nature, and include the application of fertilizers and volatilization of livestock waste (Reis et al., 2009; Ellis et al., 2013; Van Damme et al., 2014). Biomass burning, either from wildfires or from controlled burning during land-clearing operations, is also a significant source of NH_3 in rural environments. The primary source of NH_3 in urban areas are industrial emissions (e.g., NH_3 synthesis, manufacture of ammonium nitrate and urea, fluid and thermal catalytic cracking processes in petroleum refinery), though vehicular emissions can be a significant NH_3 source in some heavily populated cities (Reis et al., 2009; Lamarque et al., 2010; Yao et al., 2013; Sun et al., 2017). Vehicular NH_3 emissions are thought to be produced primarily from the reaction of nitrogen oxide with hydrogen in the presence of carbon monoxide in three-way catalysts of gasoline light duty vehicles (Barbier-Jr and Duprez, 1994; Whittington et al., 1995; Livingston et al., 2009; Suarez-Bertoa et al., 2014).

In the US, implementation of stringent emission controls on traditional anthropogenic air pollutants, such as sulfur dioxide (SO_2), nitrogen oxides (NO_x) and carbon monoxide (CO), have led to steady decreases in their emissions, and consequently their concentrations (Blanchard et al., 2013b; Xing et al., 2013). In contrast, NH_3 emissions are largely unregulated, and are projected to

increase due to increased agricultural operations to feed a growing world population (Reis et al., 2009; Ellis et al., 2013). Satellite observations showed that gas-phase NH_3 concentrations have increased substantially in US agricultural areas from 2002 to 2014 (Warner et al., 2017). More wildfires from a changing climate, or from controlled burning for land clearing for agricultural use, may also lead to increased NH_3 emissions (Reis et al., 2009; Pechony and Shindell, 2010; Warner et al., 2016). These trends suggest that NH_3 could play an increasingly important role in atmospheric chemistry.

Previous laboratory studies have shown that NH_3 can influence secondary organic aerosol (SOA) formation and processing. For example, NH_3 increases SOA mass yields in the α-pinene ozonolysis system, and is hypothesized to be due to the formation of ammonium salts from the reaction of NH_3 with organic acids (Na et al., 2007). The heterogeneous uptake of NH_3 by SOA can also lead to the formation of particulate organonitrogen compounds, a class of brown carbon species that can reduce visibility and impact climate (Laskin et al., 2010; Updyke et al., 2012; Lee et al., 2013; Laskin et al., 2015).

The southeastern U.S. is a natural outdoor laboratory for studying the effects of biogenic-anthropogenic interactions on atmospheric aerosol formation and processing. Subtropical vegetation composed mainly of mixed conifer and deciduous forests emit large quantities of biogenic volatile organic compounds (BVOCs) that can act as precursors for SOA formation (Blanchard et al., 2011; Guenther et al., 2012; Blanchard et al., 2013a). Large urban centers and small towns are surrounded by large expanses of forests and widespread rural areas with agricultural activities. Scattered within the southeastern U.S. are also coal-burning power plants and industrial facilities. Anthropogenic activities in this region emit large concentrations of VOCs, SO_2, NO_x, CO, NH_3 and aerosols (Blanchard et al., 2013c). Similar to other parts of the U.S., SO_2, CO and NO_x concentrations have decreased steadily in the southeastern U.S. due to the implementation of emission controls (Blanchard et al., 2013b). In contrast, gas-phase NH_3 concentrations have increased in the southeastern U.S. over the same time period (Saylor et al., 2015). These factors make the southeastern U.S. an intriguing place to study the influence of NH_3 on atmospheric aerosol chemistry.

We performed aerosol and gas measurements during a field study conducted in Yorkville, Georgia, U.S., in the fall of 2016, with the goal of understanding how NH_3 affects aerosol acidity

and SOA formation. The field site is surrounded by forest and agricultural land, affording an opportunity to make ambient observations in an area impacted by local emissions of BVOCs and NH_3. In this paper, we present gas and aerosol composition measurements that includes a suite of organic acids. The thermodynamic equilibrium model, ISORROPIA-II, is used to calculate particle water and pH based on measured inorganic aerosol and gas composition (Nenes et al., 1998; Fountoukis and Nenes, 2007), and these predictions are compared to observed gas-particle partitioning of NH_3, HNO_3 and organic acids. Together, these measurements are used to determine how aerosol acidity affects the mass concentration of particle-phase organic acids at this site.

2. Methods

2.1. Field site

Aerosol and gas measurements were conducted at the Yorkville, Georgia (33.929 N, 85.046 W) SouthEastern Aerosol Research and Characterization (SEARCH) field site from mid-August to mid-October 2016. This is one of the sampling sites for the Southeastern Center for Air Pollution and Epidemiology (SCAPE) study where aerosol characterization measurements were conducted in the summer and winter of 2012 (Xu et al., 2015a; Xu et al., 2015b). A detailed description of the field site can be found in Hansen et al. (2003) . This rural site is situated in a mixed forest-agriculture area approximately 55 km northwest and generally upwind of Atlanta. The immediate surrounding area is used for cattle grazing and poultry concentrated animal feeding operations (CAFOs) (Fig. S1). There are no major roads near the field site and nearby traffic emissions were negligible. A large coal-fired power plant (Plant Bowen) is situated approximately 25 km north of the site. Hence, the field site is impacted mainly by BVOC and NH_3 emissions, with occasional spikes in SO_2 and minimal influence from urban anthropogenic pollutants such as HNO_3, O_3, NO_x and CO (Fig. S2). The sampling period was characterized by moderate temperatures (24.0 °C average, 32.6 °C max, 9.5 °C min) and high relative humidities (68.9 % RH average, 100 % RH max, 21.6 % RH min). Meteorological data are shown in Fig. S3. Data reported are displayed in eastern daylight time (EDT).

2.2. Instrumentation

Instruments were housed in a temperature controlled (~20 °C) trailer during the field study. Gas-phase HNO_3, SO_2 and organic acids (formic, acetic, oxalic, butyric, glycolic, propionic,

126 valeric, malonic and succinic acids) were measured by a custom-built chemical ionization mass
127 spectrometer (CIMS) using sulfur hexafluoride ions (SF_6^-) as reagent ions. SO_2 and HNO_3 were
128 detected as fluoride adducts ($F_2SO_2^-$ and NO_3^-•HF, respectively) while the organic acids (HX) were
129 detected primarily as conjugated anions (X^-) by the quadrupole mass spectrometer (Huey et al.,
130 1995; Huey et al., 2004; Nah et al., 2018). This CIMS is referred hereafter as the SF_6-CIMS. Gas-
131 phase NH_3 was measured by an additional custom-built CIMS using protonated ethanol clusters
132 ($(C_2H_5OH)_n^+$) as reagent ions. NH_3 was detected primarily as NH_4^+ ions by the quadrupole mass
133 spectrometer (Nowak et al., 2002; Yu and Lee, 2012; You et al., 2014a). This CIMS is referred
134 hereafter as the NH_3-CIMS.

135 Since HNO_3, NH_3 and organic acids may condense on surfaces, both SF_6-CIMS and NH_3-
136 CIMS used inlet configurations that minimized wall interactions (Huey et al., 2004; Nowak et al.,
137 2006). Each CIMS was connected to an inlet (a 7.6 cm ID aluminum pipe) that protruded beyond
138 the trailer's wall by ~40 cm into the ambient air. Both inlets were ~2 m above the ground. A donut-
139 shaped ring was attached to the ambient sampling port of each pipe to curtail the influence of
140 crosswinds on the pipe's flow dynamics. Both rings were wrapped with a fine wire mesh to prevent
141 ingestion of insects. A flow of ~2800 L min^{-1} was maintained in each pipe using regenerative
142 blowers (AMETEK Windjammer 116637-03). Part of this flow (7 L min^{-1} for the SF_6-CIMS and
143 4.6 L min^{-1} for the NH_3-CIMS) was sampled through a custom-made three-way PFA Teflon valve,
144 which connected the pipe's center to the CIMS sampling orifice and could be switched
145 automatically between ambient and background measurements.

146 Background measurements were performed every 25 min for 4 min for both the SF_6-CIMS
147 and NH_3-CIMS. During each background measurement, the sampled air flow was passed through
148 an activated charcoal scrubber (Sigma Aldrich) that removed SO_2, HNO_3 and organic acids prior
149 to delivery into the SF_6-CIMS, and through a silicon phosphate scrubber (Perma Pure Inc.) that
150 removed NH_3 prior to delivery into the NH_3-CIMS. > 99 % of the targeted species were removed
151 during background measurements for both the SF_6-CIMS and NH_3-CIMS. Standard addition
152 calibrations were performed every 5 h for the SF_6-CIMS using the outputs of a 1.12 ppm $^{34}SO_2$
153 gas cylinder (Scott-Marrin Inc.) and a formic or acetic acid permeation device (VICI Metronics).
154 Calibrations for the other gases measured by the SF_6-CIMS were performed in post-field
155 laboratory work, details of which can be found in Nah et al. (2018) and SI section S1. Standard

addition calibrations were performed hourly for the NH_3-CIMS using the output of a NH_3 permeation device (KIN-TEK). The outputs of the formic and acetic acid permeation devices were measured periodically by scrubbing the output of the permeation tube in deionized water, followed by ion chromatography analysis for formate and acetate. The emission rate of the NH_3 permeation device was measured using UV optical absorption (Neuman et al., 2003).

The detection limits for species measured by the SF_6-CIMS and NH_3-CIMS were approximated from 3 times the standard deviation values (3σ) of the ion signals measured during background mode. The detection limits for HNO_3, SO_2 and the various organic acids measured by the SF_6-CIMS ranged from 1 to 60 ppt for 2.5 min integration periods, which corresponded to the length of a background measurement with a ~4 % duty cycle for each *m/z* (Table S1). Measurement uncertainties for the concentrations of HNO_3, SO_2 and the various organic acids originate mainly from calibration measurements, and were between 12 and 25 % (Table S1). The detection limit for NH_3 measured by the NH_3-CIMS was 1 ppb for 2.3 min integration periods, which corresponded to the length of a background measurement with a ~29 % duty cycle for the NH_4^+ ion. Measurement uncertainties for NH_3 concentrations were 13 %.

A high-resolution time-of-flight aerosol mass spectrometer (HR-ToF-AMS, Aerodyne Research Inc.) was used to measure the elemental composition of ambient non-refractory PM_1 (particles with aerodynamic diameters < 1 μm). Ambient air was sampled at 16.7 L min^{-1} though a URG PM_1 cyclone and then through a nafion dryer prior to delivery into the HR-ToF-AMS. Aerosols were dried to RH < 20 % to eliminate the influence of RH on the HR-ToF-AMS's particle collection efficiency. A detailed description of the HR-ToF-AMS can be found in the literature (DeCarlo et al., 2006; Canagaratna et al., 2007; Canagaratna et al., 2015). Briefly, the aerodynamic lens of the HR-ToF-AMS focused the dried submicron aerosols into a narrow beam. The aerosols were then impacted onto a heated tungsten surface (~600 °C) where they were flash vaporized. The resulting vapors were ionized by electron impact ionization (70 eV), and the ions were detected by a time-of-flight mass spectrometer. Gas-phase interferences were accounted for by subtracting the signals obtained during daily measurements of filtered, particle-free sampling air. Ionization efficiency calibrations were performed weekly using 300 nm ammonium nitrate and ammonium sulfate particles. Composition-dependent collection efficiency (CDCE) values of 0.44 to 0.55 were determined using the procedure detailed by Middlebrook et al. (2012), where CDCE

values are derived based largely on aerosol inorganic species concentrations and the relative humidity in the sampling line. In addition, a constant collection efficiency (CE) value of 0.9 was determined from the comparison of raw HR-ToF-AMS SO_4^{2-} data with other particulate SO_4^{2-} measurements performed during the study. Comparisons of aerosol mass concentrations obtained from the application of CDCE values (i.e., 0.44 to 0.55) vs. a constant CE value (i.e., 0.9) to the raw HR-ToF-AMS data are discussed in section 3.2. Uncertainties in HR-ToF-AMS measurements were estimated to be approximately 25 % (Canagaratna et al., 2007).

Particle-phase water-soluble organic acids, inorganic cations and anions were measured using two Particle-into-Liquid Sampler (PILS) systems coupled to ion chromatographs (ICs) (Orsini et al., 2003). Each PILS sampled ambient air at nominally 16.7 L min^{-1} through a URG PM_1 cyclone. Before PILS1, which was used to measure water-soluble inorganic cation and anions, two long (24 cm) URG glass annular denuders coated with sodium carbonate and phosphorous acid were used to remove acidic and basic gases. Before PILS2, which measured water-soluble organic acids, a 28 cm parallel plate carbon denuder (Sunset Lab) was used to remove organic gases (Eatough et al., 1993). In each PILS, aerosols were mixed with water vapor at ~100 °C generated from heated ultrapure deionized water (Weber et al., 2001; Orsini et al., 2003). The resulting droplets were impacted onto a plate, with the resulting liquid sample analyzed by ICs. Each IC system was calibrated at the beginning and end of the study using five multi-compound standards in order to create calibration curves. Periodically, a HEPA filter (Pall Life Sciences) was placed on the inlet to determine the background in near real-time. The measurement uncertainty for each IC system was about 10 %.

PILS1 was connected to two Dionex ICS-1500 ICs (Thermo Fisher Scientific) to measure the water-soluble inorganic ions. These two IC systems include an isocratic pump, self-regenerating anion or cation suppressor, and conductivity detector. This system will be referred hereafter as the PILS-IC. Anions were separated using a Dionex IonPac AS15 guard and analytical column (4 x 250 mm, Thermo Fisher Scientific) employing an eluent of 38 mM sodium hydroxide at a flow rate of 1.5 mL min^{-1}. Cations were separated using a Dionex IonPac CS12A guard and analytical column (4 x 250 mm, Thermo Fisher Scientific) employing an eluent of 18 mM methanesulfonic acid at a flow rate of 1 mL min^{-1}. A new chromatogram was obtained every 30

min with a sample loop fill time (i.e., ambient sample integration time) of 20 min. The limit of detection for the various anions and cations was approximately 0.01 μg m^{-3}.

PILS2 was coupled to a Dionex ICS-4000 capillary high-pressure ion chromatography (HPIC) system to measure the water-soluble organic acids. The HPIC includes an eluent generator, isocratic pump, degausser, suppressor, carbonate removal device, and conductivity detector. This system will be referred hereafter as the PILS-HPIC. The organic acids were separated using a Dionex AS11-HC-4μm capillary guard and analytical column (0.4 x 250mm, Thermo Fisher Scientific), which used a potassium hydroxide gradient separation method at a flow rate of 0.015 mL min^{-1}. A new chromatogram was obtained every 60 min with a sample loop fill time of 2 min. The limit of detection for the various organic acids was approximately 0.001 μg m^{-3}.

Particle- and gas-phase water-soluble organic carbon ($WSOC_p$ and $WSOC_g$, respectively) were measured using two Sievers 900 series total organic carbon (TOC) analyzers (GE Analytical Instruments), as described by Sullivan et al. (2004). For $WSOC_p$ measurements, ambient air was sampled at 15.2 L min^{-1} through a URG PM_1 cyclone and a parallel plate carbon denuder into a PILS coupled to the first TOC analyzer. For $WSOC_g$ measurements, ambient air was sampled at 20 L min^{-1} through a Teflon filter (45 mm diameter, 2.0 μm pore size, Pall Life Sciences) to remove particles in the air stream. This filter was changed every 3 to 4 days. The particle-free air was then directed to a MIST chamber filled with ultrapure deionized water, which scrubbed the soluble gases at an air flow rate of 20 L min^{-1}. Soluble gases with Henry's law constants greater than 10^3 mole L^{-1} atm^{-1} were scrubbed into deionized water in the MIST chamber (Spaulding et al., 2002). The resulting MIST chamber liquid sample was analyzed by the second TOC analyzer. The TOC analyzers converted the organic carbon in the liquid samples to carbon dioxide using UV radiation and chemical oxidation. The carbon dioxide formed was then measured by conductivity. The amount of organic carbon in the liquid samples is proportional to the measured increase in conductivity of the dissolved carbon dioxide. Each $WSOC_p$ and $WSOC_g$ measurement lasted 4 min. Background $WSOC_p$ and $WSOC_g$ measurements were performed for 45 min every 12 h by stopping the sample air flow and rinsing the system with deionized water. Both TOC analyzers were calibrated at the beginning and end of the study using varying concentrations of sucrose solutions to create calibration curves (as specified by the instrument manual). The limit of detections for $WSOC_p$ and $WSOC_g$ were 0.2 and 0.4 μgC m^{-3}, respectively. The measurement

uncertainties for $WSOC_p$ and $WSOC_g$ were estimated to be 10 % based on uncertainties in the TOC analyzer, sample air and liquid flows.

A suite of instruments operated by the SEARCH network provided supporting gas and aerosol measurements (Hansen et al., 2003; Edgerton et al., 2005, 2006). O_3 was measured by a UV absorption instrument (Thermo Fisher Scientific) with a temporal resolution of 1 min. NO and NO_x were measured by a chemiluminescence instrument (Thermo Fisher Scientific) with a temporal resolution of 1 min. NO_2 was obtained from the difference between NO and NO_x. CO was measured by a non-dispersive infrared absorption instrument (Thermo Fisher Scientific) with a temporal resolution of 1 min. NH_3 was measured by a denuder-based instrument (ARA) with a temporal resolution of 5 min. Comparisons of measurements by the NH_3-CIMS and denuder-based instrument will be presented in section 3.1. A filter-based particle composition monitor (ARA) provided 24 h-integrated $PM_{2.5}$ measurements of particle mass and major inorganic ions measured offline by ion chromatography. Organic carbon (OC) and elemental carbon (EC) in $PM_{2.5}$ were measured by a OCEC Analyzer (Sunset Labs) with a temporal resolution of 1 h. This analyzer determined OC by thermal optical transmittance. VOCs were measured by a gas chromatography-flame ionization detector (GC-FID, Agilent Technologies) with a temporal resolution of 1h.

2.2. Particle pH and water calculation

The thermodynamic equilibrium model ISORROPIA-II was used to determine the phase state and composition of an NH_4^+-SO_4^{2-}-NO_3^--Cl^--Na^+-Ca^{2+}-K^+-Mg^{2+}-water inorganic aerosol in equilibrium with its corresponding gas-phase species (Fountoukis and Nenes, 2007; Nenes et al., 1998). This approach was used in previous studies to determine particle water and pH in different parts of the world (Guo et al., 2015; Bougiatioti et al., 2016; Guo et al., 2016; Weber et al., 2016; Guo et al., 2017a; Guo et al., 2017c; Shi et al., 2017). The pH of an aqueous solution is defined as the negative logarithm of the hydronium ion (H_3O^+) activity on a molality basis (www.goldbook.iupac.org/html/P/P04524.html, last access: 6 July 2018):

$$pH = -\log_{10}[a(H^+)] = -\log_{10}\left[m(H^+)\gamma_m(H^+)/m^\theta\right] \quad (1a)$$

where $a(H^+)$ is the hydronium ion activity in an aqueous solution, $m(H^+)$ is the hydronium ion molality, $\gamma_m(H^+)$ is the molality-based hydronium ion activity coefficient, and m^θ is the standard molality (1 mol kg^{-1}). For simplicity, H_3O^+ is denoted here as H^+ even though we recognize that

the unhydrated hydrogen ion is rare in aqueous solutions. Since most thermodynamic equilibrium models (e.g., ISORROPIA-II, E-AIM) do not report liquid concentrations, but instead report species in terms of concentration per volume of air (e.g., µg m^{-3}, µmol m^{-3}), we have calculated the particle pH by:

$$pH = -\log_{10}\gamma_{H^+}H^+_{aq} = -\log_{10}\frac{1000\gamma_{H^+}H^+_{air}}{W_i + W_o} \cong -\log_{10}\frac{1000\gamma_{H^+}H^+_{air}}{W_i} \qquad (1b)$$

where γ_{H^+} is the hydronium ion activity coefficient (assumed to be 1), H^+_{aq} is the concentration of hydronium ions in particle water in mole L^{-1} (i.e., the density of water is assumed to be 1000 kg m^{-3}, and so pH is calculated in terms of molality), H^+_{air} (µg m^{-3}) is the hydronium ion concentration per volume of air, and W_i and W_o (µg m^{-3}) are the bulk particle water concentrations associated with inorganic and organic species per volume of air, respectively. In equation 1b, the molecular weight of H^+ is taken as 1 g mole^{-1}, and 1000 is the factor needed for unit conversion of g L^{-1} to µg m^{-3}. H^+_{air} and W_i are outputs of the ISORROPIA-II model. Previous studies have shown that particle pH values predicted using only W_i are reasonably accurate since the sensitivity of particle pH to the effects of W_o is small (Guo et al., 2015). For the southeastern U.S., Guo et al. (2015) reported that particle pH values predicted using only W_i were systematically 0.15 to 0.23 units lower than those predicted using W_i + W_o during the 2013 Southern Oxidant Aerosol Study (SOAS) and SCAPE campaigns. Given this small deviation and that organic aerosol hygroscopicity was not measured in this field study, we report particle pH only considering W_i.

ISORROPIA-II was run in "forward" mode, which assumes that aerosols are "metastable" with no solid precipitates, to predict particle pH and the partitioning of semi-volatile compounds. In "forward" mode, the model calculates the gas-particle equilibrium partitioning concentrations based on the input of the total concentration of a species (i.e., gas + particle). In "reverse" mode, the model calculates the gas-particle equilibrium partitioning concentrations based on the input of only the particle-phase concentration of a species. We used "forward" mode because the "reverse" mode is sensitive to measurement errors, which often result in large model biases in the predicted particle pH (Hennigan et al., 2015). The measured particle-phase inorganic NH_4^+, SO_4^{2-} and NO_3^- concentrations and gas-phase HNO_3 and NH_3 concentrations were used as model inputs. The "metastable" assumption is reasonable since the high RH (average RH 68.9 %) observed during the study indicated that the aerosols had likely deliquesced. We excluded data for periods where

Deleted: can be calculated as

Deleted: molarity-based

Deleted: (mole L^{-1})

Deleted: molar

Deleted: r

the RH was above 95 % since the exponential growth in particle liquid water with RH introduces large pH uncertainties (Malm and Day, 2001; Guo et al., 2015).

In using ISORROPIA-II to predict particle pH and the partitioning of semi-volatile compounds, we also assumed that the aerosols are internally mixed and that the particle pH does not change with particle size (i.e., the overall particle pH is characterized by the particle's bulk properties). As long as some small fraction of sulfate is mixed with various aerosol components, (e.g., non-volatile cations), the assumption that aerosols are completely internally mixed has a small effect on the predicted pH (Guo et al., 2017b). However, the presence of multiple organic and inorganic species in ambient aerosols may lead to multiple phases within the particle (i.e., phase separation). Consequently, this may result in the unequal distribution of inorganic species among different phases, each with its own water activity and inorganic concentration. Previous studies have shown that liquid-liquid and solid-liquid phase separations may occur for mixed organic and inorganic aerosols at low RH and organic aerosol oxygen-to-carbon atomic ratios (O/C) (Bertram et al., 2011; Song et al., 2012; You et al., 2013; You et al., 2014b; You and Bertram, 2015). Phase separations were always observed at $O/C \leq 0.5$, while no phase separation was observed at $O/C \geq 0.8$. The probability for the occurrence of phase separation decreased at higher RH for $0.5 < O/C < 0.8$. The average O/C for this field study is 0.69 ± 0.06. Organic acids were not included in the calculation of particle pH. This is reasonable since their total mass concentration was small compared to the total inorganic mass concentration. The average ratio of the organic acid mass concentration to the inorganic mass concentration is 0.25. Furthermore, Song et al. (2018) showed that including organic acid mass concentrations in thermodynamic model calculations had minor effects on particle pH if the system is in equilibrium. The validity of these assumptions and the resulting thermodynamic model predictions will be evaluated by comparing the predicted gas-particle partitioning ratios of semi-volatile inorganic compounds with measured values in section 3.3.

3. Results and Discussion

3.1. NH_3 observations

Continuous measurements of NH_3 were made using the NH_3-CIMS from 13 September to 12 October. Figures 1a and 1b show the time series and average diurnal profile of NH_3,

335 respectively. NH_3 concentrations ranged from 0.7 to 39.0 ppb (0.5 to 28.5 μg m^{-3}), and exhibited
336 consistent diurnal cycles. NH_3 was generally higher in the late mornings and early afternoons.
337 Concentrations started to increase at 07:30, which coincided with an increase in temperature at
338 sunrise (Fig. S3). Possible reasons for the morning increase include volatilization of particulate
339 ammonium and animal waste, entrainment from the residual layer where NH_3 may not have been
340 depleted, evaporation of dew or fog that contained dissolved NH_3, and emission from plant stomata
341 (Ellis et al., 2011). NH_3 decreased at 14:30, approximately 1 hour before temperature decreased,
342 and may be due to changes in the boundary layer height. However, this hypothesis cannot be tested
343 since the boundary layer height was not measured during the study. The diurnal plot does not
344 account for dilution as the boundary layer expanded, and only indicates that if emissions were
345 solely from the surface and lower concentrations aloft, these NH_3 sources were of significant
346 magnitude.

347 The average NH_3 concentration measured by the NH_3-CIMS is 8.1 ± 5.2 ppb. This is
348 approximately 2 times higher than the average NH_3 concentration (3.8 ± 2.9 ppb) measured by the
349 denuder-based instrument operated by the SEARCH network over the same time period (Fig. S4).
350 Differences in NH_3 concentrations measured by the two instruments may be due to positive and
351 negative sampling artifacts caused by differences in sampling inlets (e.g., inlet length and
352 location), frequency of calibration and background measurements, and (in the case of the denuder-
353 based instrument) possible sample contamination during chemical analysis. Discussions on how
354 differences in measured NH_3 concentrations affect PM_1 pH predictions will be presented in section
355 3.3. Nevertheless, there is a record of NH_3 concentrations measured by the denuder-based
356 instrument at this site since 2008. Just prior to, and during this study, NH_3 concentrations are
357 generally the highest observed since 2011 (Fig. S5). These elevated NH_3 concentrations may be
358 due to sporadic biomass burning episodes caused by elevated temperatures and widespread
359 drought across the southeastern U.S. in 2016 (Park Williams et al., 2017; Case and Zavodsky,
360 2018).

361 The NH_3-CIMS measurements are examined with the meteorological data to gain insights
362 on the primary NH_3 sources during the sampling period. To account for wind speed, the 1-hour
363 averaged NH_3 concentrations are first multiplied by their corresponding 1-hour averaged wind
364 speeds. These normalized NH_3 concentrations are then used to construct a wind direction polar

plot showing the average normalized NH_3 concentration per 10 degrees bin (Fig. 1c). The wind direction polar plot shows that the normalized NH_3 is approximately 2 times greater than the average when air masses are transported from the south-east, the general direction of the poultry CAFOs located approximately 2 km from the field site (Fig. S1), which are known for high NH_3 emissions. This conclusion is reaffirmed by NH_3 measurements by the SEARCH network's denuder-based instrument.

NH_3 concentrations measured by the two instruments in this study are substantially higher than those measured in three recent field studies conducted in the continental U.S.: 2010 California Nexus (CalNex) study, 2013 Southeast Nexus (SENEX) study and 2013 SOAS study (see Table 1). The differences in NH_3 may be attributed to differences in land use, proximity to CAFOs and meteorological conditions. The high NH_3 concentrations in this study allow us to make ambient observations of the effect of NH_3 on particle acidity and the gas-particle partitioning of semi-volatile inorganic and organic compounds, and compare them with previous studies.

3.2. PM_1 composition

The aerosol inorganic chemical composition was measured by several instruments during this study. The HR-ToF-AMS, PILS-IC and PILS-HPIC measured the composition of PM_1, while a filter-based particle composition monitor measured the composition of $PM_{2.5}$. Comparisons of aerosol SO_4^{2-}, NO_3^- and NH_4^+ mass concentrations obtained from the application of CDCE values to the raw HR-ToF-AMS data are compared to those measured by the other three instruments in Fig. S6. NH_4^+ measurements by the PILS-IC are not available for comparison due to denuder breakthrough that occurred during the study.

SO_4^{2-} measurements by the various instruments are generally well correlated with each other, with R^2 values ranging from 0.64 to 0.92. Although PM_1 SO_4^{2-} measurements by the two PILS systems show good agreement with each other, HR-ToF-AMS CDCE-applied SO_4^{2-} measurements are approximately two times higher than the PILS and filter measurements. Similar systematic differences are also observed for NO_3^- and NH_4^+ measurements. NO_3^- and NH_4^+ measurements by the four instruments are moderately correlated (R^2 = 0.54 to 0.79 and R^2 = 0.94, respectively). NO_3^- measurements by the PILS and filter systems are mostly similar; however, HR-ToF-AMS CDCE-applied PM_1 NO_3^- and NH_4^+ measurements are approximately three times and

two times higher than the PILS and filter measurements. One possible reason is that the calculated CDCE is lower due to organics dominating the aerosol composition during the study (average of 74.2 ± 7.9 % of the non-refractory PM_1 mass concentration). Lee et al. (2015) suggested that a high organic mass fraction may impede the complete efflorescence of aerosols when they are passed through the drier prior to delivery into the HR-ToF-AMS, thus reducing the particle bounce and increasing the CE value. Hence, we estimated HR-ToF-AMS PM_1 mass concentrations that would be consistent with PILS and filter measurements by multiplying all the raw HR-ToF-AMS data by a constant CE value of 0.9, which was obtained from comparisons of the raw HR-ToF-AMS SO_4^{2-} data with PILS-IC and PILS-HPIC SO_4^{2-} measurements. The constant CE-applied HR-ToF-AMS data is used in all our subsequent analyses.

Figure 2 shows the time series and average diurnal profiles of non-refractory PM_1 species. The average non-refractory PM_1 organics, SO_4^{2-}, NO_3^- and NH_4^+ mass concentrations are 5.0 ± 2.3, 1.6 ± 0.4, 0.2 ± 0.1 and 0.4 ± 0.2 μg m^{-3}, respectively. Organics are the dominant non-refractory PM_1 species, accounting for 74.2 ± 7.9 % of the non-refractory PM_1 mass concentration during the field study. Organic aerosol mass concentration was slightly higher at night, which is likely caused by changes in the boundary layer height, emission sources and SOA formation processes (Xu et al., 2015b). Previous studies have shown that nighttime SOA production in the Southeastern U.S. is largely attributed to nitrate radical oxidation and ozonolysis of monoterpenes, which are abundant at night (Pye et al., 2015; Xu et al., 2015a; Xu et al., 2015b; Lee et al., 2016; Zhang et al., 2018). Specifically, the nitrate radical oxidation of some monoterpenes (e.g., β-pinene) could form low volatility organic nitrates that are condensable and could contribute substantially to the nocturnal organic aerosol mass (Boyd et al., 2015; Boyd et al., 2017; Ng et al., 2017). Apportionment of organic aerosol sources will be discussed in an upcoming publication. SO_4^{2-} is the second most abundant non-refractory PM_1 species (16.3 ± 5.7 % mass fraction), followed by NH_4^+ (5.9 ± 2 % mass fraction) and NO_3^- (3.6 ± 2.2 % mass fraction). SO_4^{2-} mass concentration peaked in the afternoon due to enhanced SO_2 photooxidation (Weber et al., 2003). The NO_3^- mass concentration measured by the HR-ToF-AMS is the nitrate functional group (-ONO_2) present on organic and inorganic nitrates. Hence, the diurnal profile of the NO_3^- mass concentration in Fig. 2 has contributions from both organic and inorganic nitrates. The mass concentrations of organic and inorganic nitrates increased after sunset and peaked at sunrise (Fig. S7), likely due to the formation of organic nitrates from nighttime NO_3 chemistry and increased

gas-to-particle partitioning of organic and inorganic nitrates as temperature decreased (Xu et al., 2015a; Xu et al., 2015b). Quantification and characterization of organic nitrates based on HR-ToF-AMS and PILS-IC PM_1 NO_3^- measurements will be discussed in a future publication. NH_4^+ mass concentration has moderate diurnal variations with marginally higher concentrations in the afternoon, likely due to the contrasting day/night phases of ammonium sulfate and ammonium nitrate formation. SO_4^{2-}, NO_3^- and NH_4^+ molar concentrations indicated that NH_4^+ is mainly associated with SO_4^{2-} in PM_1.

3.3. PM_1 pH predictions

CIMS HNO_3 and NH_3 data, HR-ToF-AMS PM_1 SO_4^{2-} and NH_4^+ data, PILS-IC PM_1 NO_3^- and non-volatile cation (Cl^-, Na^+, Ca^{2+}, K^+ and Mg^{2+}) data, measured temperature and RH are used as ISORROPIA-II model inputs to predict PM_1 W_i and pH from 13 September to 6 October. Figure 3 shows the time series and average diurnal profiles of ISORROPIA-predicted PM_1 W_i and pH. PM_1 are highly acidic with pH values ranging from 0.9 to 3.8, and an average pH of 2.2 ± 0.6. The average PM_1 pH was 2.5 ± 0.6 during periods where the NH_3 concentration was higher than 13.3 ppb (i.e., average NH_3 concentration + 1 standard deviation = 8.1 + 5.2 = 13.3 ppb). The PM_1 pH values in this study are generally similar to those reported by Guo et al. (2015) at the same field site during winter 2012. Our observation that PM_1 are acidic despite the high NH_3 concentrations in this study is consistent with previous studies showing that particle pH has weak sensitivities to wide NH_3 and SO_4^{2-} mass concentration ranges due to pH buffering caused by the partitioning of NH_3 between the gas and particle phases (Weber et al., 2016; Guo et al., 2017c). This weak particle pH sensitivity also explains the small changes in PM_1 pH values (about 10 % lower, Fig. S8) when NH_3 measurements by the SEARCH network denuder-based instrument are used in ISORROPIA-II calculations (instead of NH_3-CIMS measurements).

PM_1 pH varied by approximately 1.4 units throughout the day. W_i has an average value of 1.6 ± 1.7 μg m^{-3}. PM_1 W_i and pH showed similar diurnal profiles, with both peaking in the mid-morning and reaching their minima in the mid-afternoon. These diurnal trends are consistent with those previously reported by Guo et al. (2015) for PM_1 measured during the summer and winter in different parts of the southeastern U.S. Also shown in Fig. 3b is the diurnal profile of H_{air}^+, which peaked in the mid-afternoon. The W_i and H_{air}^+ maximum/minimum ratios are comparable (6.5 and

5.3, respectively), thus indicating that the diurnal variation in particle pH is driven by both W_i and H^+_{air}.

The average PM_1 pH for this study is about 1 unit higher than those for the SENEX and SOAS campaigns (Table 1), and is likely due to the much higher abundance of NH_3 in this study. The average NH_3 mass concentration in this study is approximately 49 times and 15 times higher than those in the SENEX and SOAS campaigns, respectively. The average PM_1 pH for this study is similar to that for the CalNex campaign even though the average NH_3 mass concentration in this study is only approximately 4 times higher than that in the CalNex campaign (Guo et al., 2017a). This may be due, in part, to PM_1 SO_4^{2-} and NO_3^- mass concentrations at CalNex being approximately 2 times and 18 times larger than those of this study, respectively. Aerosol inorganic SO_4^{2-} and NO_3^- species are hygroscopic species. The much higher NO_3^- mass concentrations in the CalNex campaign (due, in part, to high NO_x emissions) increased particle W_i substantially, which diluted H^+ and raised particle pH, resulting in more gas-to-particle partitioning of NO_3^-, and eventually leading to pH levels similar to those observed in this study. This type of feedback does not happen in the southeastern U.S. where non-volatile SO_4^{2-} dominates the uptake of particle water. It is also possible that the higher RH and lower temperatures during the CalNex campaign (relative to this study) contributed to high particle W_i, which diluted H^+ and raised particle pH levels similar to those observed in this study.

The validity of this study's thermodynamic model predictions is evaluated by comparing the predicted gas-particle partitioning ratios of semi-volatile inorganic compounds (i.e., NO_3^- and NH_4^+) with measured values (Fig. S9). CIMS HNO_3 and NH_3 data, PILS-IC NO_3^- and HR-ToF-AMS NH_4^+ data are used in this comparison. $\varepsilon(NO_3^-)$ and $\varepsilon(NH_4^+)$ are defined as the particle-phase molar concentration divided by the total molar concentration (gas + particle), i.e., $\varepsilon(NO_3^-) = NO_3^- / (HNO_3 + NO_3^-)$ and $\varepsilon(NH_4^+) = NH_4^+ / (NH_3 + NH_4^+)$. Predicted NH_3, NH_4^+ and $\varepsilon(NH_4^+)$ values are generally within 10 % of and are highly correlated (R^2 = 0.96 to 0.99) with measured values (Fig. S9). While predicted HNO_3 values generally agreed with measurements, substantial scatter can be seen between the predicted and measured values for NO_3^- and $\varepsilon(NO_3^-)$. This scatter can be attributed, at least in part, to uncertainties brought about by the low PM_1 NO_3^- mass concentrations and effects of coarse mode cations (e.g., Na^+, Ca^{2+}, K^+ and Mg^{2+}) on fine mode HNO_3-NO_3^- gas-particle equilibrium (i.e., HNO_3 can partition to both fine and coarse modes, thereby affecting fine

484 mode NO_3^- concentrations; no such effect occurs for NH_3-NH_4^+ gas-particle equilibrium). In
485 general, the overall good agreement between model predictions and measurements indicated that
486 our assumptions that aerosols are metastable (i.e., aerosols are supersaturated aqueous droplets)
487 with no phase separation for the thermodynamic calculations are reasonable for the conditions of
488 this study, and do not affect model predictions.

489 The molar fractions of NO_3^- and NH_4^+ in the particle phase (i.e., $\varepsilon(NO_3^-)$ and $\varepsilon(NH_4^+)$)
490 measured in this study are compared with those measured during the CalNex, SENEX and SOAS
491 campaigns. Figure 4 shows the measured $\varepsilon(NO_3^-)$ and $\varepsilon(NH_4^+)$ values as a function of their
492 ISORROPIA-predicted particle pH for the various field studies. For each field study, only a subset
493 of the data is chosen for this comparison ($1 \le W_i \le 4$ μg m^{-3} and 15 °C ≤ temperature ≤ 25 °C) to
494 reduce the effects of variability of W_i and temperature on gas-particle partitioning for comparison
495 with the calculated S (or sigmoidal) curves, which are calculated based on W_i = 2.5 μg m^{-3} and
496 temperature = 20 °C. The S curves for HNO_3-NO_3^- and NH_3-NH_4^+ partitioning as a function of
497 particle pH are also plotted as solid lines. The S curves are calculated based on the solubility and
498 dissociation of NO_3^- and NH_4^+ species in water:

$$\varepsilon(NO_3^-) = \frac{H^*_{HNO_3} RTW_i \times 0.987 \times 10^{-14}}{\gamma_{H^+}\gamma_{NO_3^-} 10^{-pH} + H^*_{HNO_3} RTW_i \times 0.987 \times 10^{-14}} \quad (2)$$

$$\varepsilon(NH_4^+) = \frac{\frac{\gamma_{H^+} 10^{-pH}}{\gamma_{NH_4^+}} H^*_{NH_3} RTW_i \times 0.987 \times 10^{-14}}{1 + \frac{\gamma_{H^+} 10^{-pH}}{\gamma_{NH_4^+}} H^*_{NH_3} RTW_i \times 0.987 \times 10^{-14}} \quad (3)$$

499 where $H^*_{HNO_3}$ and $H^*_{NH_3}$ (mole^2 kg^{-2} atm^{-1}) are equilibrium constants and are the products of the
500 Henry's law constant and the dissociation constant of HNO_3 and NH_3, respectively, R is the gas
501 constant (8.314 m^3 Pa K^{-1} mol^{-1}), T is temperature (K), and γ_i's are activity coefficients. $H^*_{HNO_3}$
502 and $H^*_{NH_3}$ values at 20 °C are calculated using equations found in Clegg and Brimblecombe (1990)
503 and Clegg et al. (1998), respectively. Activity coefficients predicted by ISORROPIA-II are
504 $\gamma_{H^+-NO_3^-} = \sqrt{\gamma_{H^+}\gamma_{NO_3^-}}$ = 0.28, γ_{H^+} = 1 and $\gamma_{NH_4^+}$ = 1. Derivations of the analytically calculated S
505 curves for $\varepsilon(NO_3^-)$ and $\varepsilon(NH_4^+)$ in equations 2 and 3 can be found in Guo et al. (2017a). As shown
506 in Fig. 4, the measured $\varepsilon(NO_3^-)$ and $\varepsilon(NH_4^+)$ values for the four field studies all generally
507 converged on the calculated S curves. The higher particle pH values in this study and the CalNex

campaign relative to those for the SENEX and SOAS campaigns resulted in less NH_3 and more HNO_3 partitioned to the particle phase, as predicted by these simple analytical expressions. A similar analysis will be performed for the organic acids in section 3.5.

3.4. WSOC and water-soluble organic acids

The time series and average diurnal profiles of $WSOC_g$ and $WSOC_p$ are shown in Fig. S10. The average $WSOC_g$ mass concentration (3.6 ± 2.7 μgC m^{-3}) is roughly four times higher than that of $WSOC_p$ (1.0 ± 0.6 μgC m^{-3}). The diurnal profile of $WSOC_p$ is somewhat flat, likely due to various organic aerosol sources having different water solubility and diurnal cycles, and compensating each other throughout the day (Xu et al., 2015b; Xu et al., 2017). In contrast, $WSOC_g$ displayed strong diurnal variations. $WSOC_g$ increased at 07:30, which coincided with the sharp increase in solar irradiance (Fig. S3). $WSOC_g$ decreased at 21:30, approximately 2 hours after sunset. Also shown in Fig. S10 are the time series and average diurnal profile of the mass fraction of total WSOC in the particle phase, i.e., $F_p = WSOC_p / (WSOC_p + WSOC_g)$. The peak F_p coincided with the minima of $WSOC_g$ at 07:30.

The average $WSOC_g$ and $WSOC_p$ (3.6 ± 2.7 μgC m^{-3} and 1.0 ± 0.6 μgC m^{-3}) are slightly lower than those measured during the SOAS campaign (SOAS $WSOC_g = 4.9$ μgC m^{-3} and $WSOC_p = 1.7$ μgC m^{-3}) (Xu et al., 2017). While the diurnal profiles of $WSOC_p$ in both studies are flat, the diurnal profiles of $WSOC_g$ measured in the two studies are different. $WSOC_g$ measured in the SOAS study decreased at sunset, while $WSOC_g$ measured in this study decreased 2 hours after sunset. Differences in $WSOC_g$ diurnal profiles in the two studies are likely due to differences in emission sources as a result of different sampling periods (SOAS was in early summer and this study was in early fall), land use and/or land cover. The ratio of $WSOC_p$ to OC for this study was estimated at 30 %, but this comparison is imprecise because $WSOC_p$ was PM_1 and OC was $PM_{2.5}$ (refer to Fig. S11 and SI section S2).

Figure 5 shows the time series of particle- and gas-phase concentrations of formic, acetic, oxalic, malonic, succinic, glutaric and maleic acids. Their diurnal profiles are shown in Fig. 6. Gas-phase measurements of glutaric and maleic acids are not available. Gas-phase measurements of butyric, glycolic, propionic and valeric acids were also measured during the study and have

been presented in Nah et al. (2018), but will not be discussed here since their particle-phase measurements are not available.

Assuming that all the measured organic acids are completely water-soluble, 30 % of the $WSOC_g$ is comprised of these organic acids (Nah et al., 2018). Formic and acetic acids are the most abundant gas-phase organic acids, with averages of 2.2 ± 1.6 and 1.9 ± 1.3 μg m^{-3}, respectively. The average carbon mass fraction of $WSOC_g$ comprised of formic and acetic acids are 7 and 13 %, respectively. All the gas-phase organic acids displayed strong and consistent diurnal cycles, with higher concentrations being measured during warm and sunny days. Their concentrations start to increase at sunrise (at 07:30), building to a peak between 15:30 and 19:30, then decrease overnight.

Nah et al. (2018) previously showed that the measured gas-phase organic acids during the study, including oxalic acid, likely have the same or similar sources. Poor correlations between gas-phase organic acid concentrations and those of anthropogenic pollutants (HNO_3, SO_2, CO and O_3) indicated that these organic acids are not due to anthropogenic emissions, and are likely biogenic in nature. Biogenic emissions of gas-phase organic acids and/or their BVOC precursors are elevated at high temperatures, resulting in higher organic acid concentrations during warm and sunny days. For example, isoprene, which is the dominant BVOC in Yorkville, has a somewhat similar diurnal profile as the organic acids. In addition, the concentration of isoprene is moderately correlated with those of formic and acetic acids (Fig. S10 of Nah et al., 2018), which are known products of isoprene photooxidation. Some of these gas-phase organic acids may also be formed in the particle phase during organic aerosol photochemical aging, with subsequent volatilization into the gas phase. The gas-particle partitioning of organic acids likely depends on thermodynamic conditions, which are controlled by particle pH and W_i and meteorological conditions as will be shown in section 3.5.

The measured particle-phase water-soluble organic acids contributed on average 6 % to the HR-ToF-AMS-measured organic aerosol mass concentration. The average carbon mass fraction of $WSOC_p$ comprised of these organic acids is 4 %. Previous studies have shown that particle-phase organic acids found in rural environments are oxidation products of gas-phase aliphatic monocarboxylic acids, which are formed in the photochemical oxidation of biogenic unsaturated fatty acids and other BVOC precursors (Kawamura and Gagosian, 1987; Kawamura and Ikushima,

1993; Kerminen et al., 2000; Kawamura and Bikkina, 2016). These particle-phase organic acids can also be produced during the multiphase photochemical aging of ambient organic aerosols (Ervens et al., 2004; Lim et al., 2005; Sorooshian et al., 2007; Sorooshian et al., 2010).

Oxalate is the most abundant measured particle-phase water-soluble organic acid anion (contributing on average 26 % to the total particle-phase organic acid mass concentration), with mass concentrations ranging from 0.01 to 0.34 μg m^{-3} and a average of 0.07 ± 0.05 μg m^{-3}. Acetate (average of 0.06 ± 0.03 μg m^{-3}) and formate (average of 0.05 ± 0.03 μg m^{-3}) are the second and third most abundant measured particle-phase water-soluble organic acid anions, respectively. Particle-phase formate, acetate and maleate showed weak diurnal variations, and may be due, in part, to various emission sources having different diurnal cycles and compensating each other throughout the day. Particle-phase oxalate, malonate and succinate peaked in the mid- to late afternoon, while glutarate generally peaked in the mid-morning. This suggests that while the production of these organic acids is photochemically-driven, they may have different BVOC precursors and/or different photochemical production pathways. In addition, since oxalic (C_2), malonic (C_3), succinic (C_4) and glutaric (C_5) acids belong to the same homologous series of organic diacids, it is possible that the photochemical aging of particle-phase glutaric acid resulted in the formation of its successive homologues via the cleavage of C-C bonds. Hence, organic aerosol photochemical aging may also have contributed to the diurnal profiles of particle-phase oxalate, malonate, succinate and glutarate.

3.5. Gas-particle partitioning of organic acids

The online and simultaneous measurements of gas- and particle-phase organic acid mass concentrations provided the opportunity to study gas-particle partitioning behavior of semi-volatile organic compounds with respect to particle pH, as is more commonly done with semi-volatile inorganic species (see section 3.3). Since formic, acetic and oxalic acids are the three most abundant measured organic acids present in the gas and particle phases, we focus on the gas-particle partitioning behaviors of these three organic acids. The average molar fractions (± 1 standard deviation) of formic, acetic and oxalic acid in the particle phase (i.e., $\varepsilon(HCOO^-)$, $\varepsilon(CH_3CO_2^-)$ and $\varepsilon(C_2O_4^{2-})$) are 3.6 ± 3.6 %, 5.8 ± 5.0 % and 73.7 ± 9.8 %, respectively. The uncertainties of these ratios for formic, acetic and oxalic acids are 16, 16 and 17 %, respectively,

595 which are obtained from the propagation of their SF_6-CIMS and PILS-HPIC measurement
596 uncertainties.

597 **3.5.1. Oxalic acid**

598 To investigate the factors affecting oxalic acid gas-particle partitioning, the equation for
599 the S curve describing the dependence of oxalic acid gas-particle partitioning (i.e., $\varepsilon(C_2O_4^{2-}) = C_2O_4^{2-} / (C_2H_2O_4 + C_2O_4^{2-})$) on particle pH is derived. As shown in SI section S3, the analytically
601 calculated S curve for $\varepsilon(C_2O_4^{2-})$ can be simplified to:

602 $$\varepsilon(C_2O_4^{2-}) \cong \frac{H_{C_2H_2O_4} W_i RT \left(\frac{\gamma_H + \gamma_{C_2HO_4^-}}{\gamma_{C_2H_2O_4}} 10^{-pH} + K_{a1}\right) \times 0.987 \times 10^{-14}}{\gamma_{H^+} \gamma_{C_2HO_4^-} 10^{-pH} + H_{C_2H_2O_4} W_i RT \left(\frac{\gamma_H + \gamma_{C_2HO_4^-}}{\gamma_{C_2H_2O_4}} 10^{-pH} + K_{a1}\right) \times 0.987 \times 10^{-14}} \quad (4)$$

603 where $H_{C_2H_2O_4}$ (mole L^{-1} atm^{-1}) is the Henry's law constant for oxalic acid, K_{a1} (mole L^{-1}) is the
604 first acid dissociation constant for oxalic acid, R is the gas constant (8.314 m^3 Pa K^{-1} mol^{-1}), T is
605 temperature (K), and γ_i's are activity coefficients. We used the web version of AIOMFAC
606 (www.aiomfac.caltech.edu) (Zuend et al., 2008; Zuend et al., 2011; Zuend et al., 2012) to compute
607 an average $\gamma_{C_2H_2O_4}$ value of 0.0492. Since AIOMFAC does not predict $\gamma_{H^+}\gamma_{C_2HO_4^-}$, we assumed
608 that $\gamma_{H^+}\gamma_{C_2HO_4^-} = \gamma_{H^+}\gamma_{NO_3^-}$, and used the ISORROPIA-predicted $\gamma_{H^+}\gamma_{NO_3^-}$ value of 0.07. We used
609 the average of $H_{C_2H_2O_4}$ values provided by Clegg et al. (1996), Compernolle and Muller (2014)
610 and Saxena and Hildemann (1996) (6.11 x 10^8 mole L^{-1} atm^{-1} at 25 °C), and accounted for the
611 effect of temperature using equation 19 in Sander (2015). Although K_{a1} also depends on
612 temperature, we used the K_{a1} value at 25 °C (5.62 x 10^{-2} mole L^{-1}, (Haynes, 2014)) for all the
613 oxalic acid S curve calculations since equations that compute K_{a1} values for pure aqueous oxalic
614 acid solutions at different temperatures are not available in the literature. In addition, the
615 temperatures observed in this study were close to 25 °C (study-average temperature = 23.4 ± 4.0
616 °C).

617 Different S curves for $\varepsilon(C_2O_4^{2-})$ are calculated using 1-hour average values obtained from
618 the diurnal profiles of temperature and W_i (specifically at 00:30, 06:30 and 12:30). The shape of
619 the S curve changes with the time of day due to the diurnal variations of temperature and W_i (Fig
620 S12 and SI section S3). The S curves for $\varepsilon(C_2O_4^{2-})$ are very different from those of other acids,

such as $\varepsilon(NO_3^-)$ (shown in Fig. 4b). From the S curves for $\varepsilon(C_2O_4^{2-})$, which are calculated using conditions in this study, some molar fraction of oxalic acid is always expected to be present in the particle phase, even at low particle pH (i.e., the S curve does not go to zero at low pH). In contrast, HNO_3 is expected to be present primarily in the gas phase at low particle pH (i.e., pH < 1) under similar temperature and W_i conditions. This is due primarily to differences in the Henry's law constants for the two acids. H_{HNO_3} (2.57 x 10^5 mole L^{-1} atm^{-1}) at 23.4 °C is three orders of magnitude smaller than $H_{C_2H_2O_4}$ (7.27 x 10^8 mole L^{-1} atm^{-1}) (Clegg and Brimblecombe, 1990; Sander, 2015). This means that some undissociated form of oxalate can be found in the particle phase at any pH, and the molar fraction of this form increases with particle W_i (see Fig. S12). Oxalic acid's very high Henry's law constant combined with the W_i conditions in this study ensures that some fraction of the organic acid will be in the particle phase regardless the particle pH.

Figure 7 compares the measured $\varepsilon(C_2O_4^{2-})$ vs. ISORROPIA-predicted PM_1 pH to the analytically calculated S curves(s). The S curve is calculated based on the average temperature and W_i from 13 September to 6 October (23.4 ± 4.0 °C and 1.6 ± 1.7 μg m^{-3}, respectively). We also calculated the "upper" and "lower" bounds of this S curve based on one standard deviation from the average temperature and average W_i. Temperature = 27.4 °C and W_i = 0.5 μg m^{-3} are used for calculations of the "lower" bound, while temperature = 19.4 °C and W_i = 3.3 μg m^{-3} are used for calculations of the "upper" bound. For the ambient data, a range in W_i (0.5 to 4 μg m^{-3}) and temperature (15 to 31 °C) is chosen to be close to the analytical calculation. As shown in Fig. 7, the measured $\varepsilon(C_2O_4^{2-})$ generally converged around the S curve calculated using the average temperature and W_i values. Although there is some scatter, the measured ratios are mostly within the "upper" and "lower" bounds of the S curve.

Since the measured $\varepsilon(C_2O_4^{2-})$ are in general agreement with the analytically calculated S curve (Fig. 7), we can use the S curve to understand qualitatively how high NH_3 events at the site affect oxalic acid gas-particle partitioning. Here we define high NH_3 events as periods where the NH_3 concentration was higher than 13.3 ppb (which is the average NH_3 concentration + 1 standard deviation). As discussed in section 3.3, the PM_1 pH during high NH_3 events is 2.5 ± 0.6, which is slightly higher than the average PM_1 pH of 2.2 ± 0.6. Based on the S curve calculated using the

650 average temperature and W_i values, $\varepsilon(C_2O_4^{2-})$ increases from 81 % to 89 % when particle pH
651 increases from 2.2 to 2.5. While this result indicates that high NH_3 concentrations can raise the
652 particle pH sufficiently such that it can promote gas-to-particle partitioning of oxalic acid, this is
653 not always the case. Specifically, increasing the particle pH from -2 (or lower) to 1 will not result
654 in a significant increase in $\varepsilon(C_2O_4^{2-})$. Therefore, whether or not particle pH, and consequently
655 oxalic acid gas-particle partitioning, is sensitive to NH_3 concentration depends strongly on particle
656 pH values.

657 We also examined how well the analytically calculated S curve for $\varepsilon(C_2O_4^{2-})$ captures
658 diurnal variations of the measured $\varepsilon(C_2O_4^{2-})$. The ambient data is divided into two 12 hour sets
659 (08:00 to 19:59 and 20:00 to 07:59) based on the diurnal profile of solar irradiance. Two S curves
660 and their corresponding "upper" and "lower" bounds are calculated based on the average
661 temperature and W_i of the two data sets, and are subsequently compared to the ambient data. As
662 shown in Fig. S13, the measured $\varepsilon(C_2O_4^{2-})$ in both data sets are generally consistent with predicted
663 values.

664 A number of inferences can be drawn from the overall good agreement between the
665 predicted and measured molar fractions of oxalic acid in the particle phase in Figs. 7 and S13. Our
666 assumptions regarding the activity coefficients, Henry's law constant and acid dissociation
667 constants used in the S curve calculations of $\varepsilon(C_2O_4^{2-})$ are reasonable for the conditions of this
668 study (or are at least self-consistent). Analytically calculated S curves are a simple way of
669 exploring how the gas-particle partitioning of semi-volatile inorganic and organic compounds in
670 the atmosphere are affected by the compound's physicochemical properties (e.g., Henry's law
671 constants and acid dissociation constants), temperature, W_i and pH. Overall, these results indicate
672 that particle-phase oxalate is in equilibrium with gas-phase oxalic acid, and that particle pH can
673 influence particle-phase oxalate concentrations. It also showed that particle-phase oxalate can be
674 found over a broad pH range, and that the presence of oxalate does not necessarily provide insights
675 of the particle pH. Because of its high Henry's law constant, particle-phase oxalate can be found
676 in aerosols even at extremely low pH values (i.e., the flat region in Fig. 7), although our data cannot
677 be used to test this since ambient particle pH values in this study are too high.

678 **3.5.2 Formic and acetic acids**

Similar comparisons between the predicted and measured $\varepsilon(HCOO^-)$ and $\varepsilon(CH_3CO_2^-)$ can also be made. Derivation of the equations for S curves describing the dependence of formic and acetic acid gas-particle partitioning (i.e., $\varepsilon(HCOO^-)$ = $HCOO^-$ / ($HCOOH$ + $HCOO^-$) and $\varepsilon(CH_3CO_2^-)$ = $CH_3CO_2^-$ / (CH_3CO_2H + $CH_3CO_2^-$), respectively) on particle pH are similar to that of HNO_3 since they are monoprotic acids:

$$\varepsilon(HCOO^-) = \frac{H_{HCOOH} W_i RT \left(\frac{\gamma_H + \gamma_{HCOO^-}}{\gamma_{HCOOH}} 10^{-pH} + K_{a1}\right) \times 0.987 \times 10^{-14}}{\gamma_H + \gamma_{HCOO^-} 10^{-pH} + H_{HCOOH} W_i RT \left(\frac{\gamma_H + \gamma_{HCOO^-}}{\gamma_{HCOOH}} 10^{-pH} + K_{a1}\right) \times 0.987 \times 10^{-14}} \quad (5)$$

$$\varepsilon(CH_3CO_2^-) = \frac{H_{CH_3CO_2H} W_i RT \left(\frac{\gamma_H + \gamma_{CH_3CO_2^-}}{\gamma_{CH_3CO_2H}} 10^{-pH} + K_{a1}\right) \times 0.987 \times 10^{-14}}{\gamma_H + \gamma_{CH_3CO_2^-} 10^{-pH} + H_{CH_3CO_2H} W_i RT \left(\frac{\gamma_H + \gamma_{CH_3CO_2^-}}{\gamma_{CH_3CO_2H}} 10^{-pH} + K_{a1}\right) \times 0.987 \times 10^{-14}} \quad (6)$$

where H_{HCOOH} and $H_{CH_3CO_2H}$ (mole L^{-1} atm^{-1}) are the Henry's law constants for formic and acetic acid, K_{a1}'s (mole L^{-1}) are the first acid dissociation constants, R is the gas constant (8.314 m^3 Pa K^{-1} mol^{-1}), T is temperature (K), and γ_i's are activity coefficients. We used the web version of AIOMFAC (www.aiomfac.caltech.edu) (Zuend et al., 2008; Zuend et al., 2011; Zuend et al., 2012) to compute average γ_{HCOOH} and γ_{CH_3COOH} values of 0.334 and 2.150, respectively. Similar to the case of oxalic acid, we assumed that $\gamma_{H^+}\gamma_{HCOO^-}$ = $\gamma_{H^+}\gamma_{CH_3COO^-}$ = $\gamma_{H^+}\gamma_{NO_3^-}$, and used the ISORROPIA-predicted $\gamma_{H^+}\gamma_{NO_3^-}$ value of 0.07. Temperature-dependent H_{HCOOH} and $H_{CH_3CO_2H}$ values are obtained from Sander (2015) using the same methodology employed to determine temperature-dependent $H_{C_2H_2O_4}$ values. We used K_{a1} values at 25 °C (1.78 x 10^{-4} mole L^{-1} for formic acid, and 1.75 x 10^{-5} mole L^{-1} for acetic acid (Haynes, 2014)) for the S curve calculations.

S curves for $\varepsilon(HCOO^-)$ and $\varepsilon(CH_3CO_2^-)$ calculated based on temperature = 23.4 °C and W_i = 1.6 μg m^{-3} can be seen in Fig. 8. Practically no formic or acetic acids are predicted to partition to the particle phase (relative to oxalic acid) for the range of PM_1 pH calculated in this study. This is due to significant differences in the Henry's law constants and acid dissociation constants for the three organic acids. H_{HCOOH} and $H_{CH_3CO_2H}$ (9540 and 5370 mole L^{-1} atm^{-1}, respectively) at 23.4 °C are substantially smaller than $H_{C_2H_2O_4}$ (7.27 x 10^8 mole L^{-1} atm^{-1}) (Sander, 2015). The K_{a1} values for formic and acetic acids (1.78 x 10^{-4} and 1.75 x 10^{-5} mole L^{-1}, respectively) are also considerably smaller than the K_{a1} value for oxalic acid (5.62 x 10^{-2} mole L^{-1}) (Haynes, 2014). Note

that H_{HNO_3} is between that of $H_{C_2H_2O_4}$ and those of H_{HCOOH} and $H_{CH_3CO_2H}$ (compare Fig. 4b with Figs. 7 and 8).

As shown in Fig. 8, higher than expected levels of formate and acetate are observed in the particle phase. This has also been reported in previous studies (Liu et al., 2012). Laboratory tests showed that the disagreement cannot be explained by positive biases in the particle-phase formate and acetate PILS-HPIC measurements resulting from less than 100 % gas removal by the carbon denuder. The measured denuder efficiency for formic acid was ≥ 99.97% (SI section S4). The possibility that formic and acetic acid dimers in the aqueous phase (Schrier et al., 1964; Gilson et al., 1997; Chen et al., 2008) may result in higher than predicted molar fractions of formate and acetate in the particle phase was explored, but also could not explain the observed gas-particle partitioning of these acids (SI section S5). The disagreement could be due to incorrect Henry's law constants for formic and acetic acids. However, the Henry's law constants for formic and acetic acid would have to be ~10^4 times and ~3 x 10^5 times larger than their literature values, respectively, in order for their S curves to match our measured molar fractions of formic and acetic acid in the particle phase. In addition, formic and acetic acids may not be internally mixed with most of the other PM_1 aerosol components (e.g., SO_4^{2-}, NO_3^-, NH_4^+, $C_2O_4^{2-}$), and thus are not associated with acidic aerosols, as assumed above. They may instead be associated with aerosols largely composed of non-volatile cations and have a pH closer to neutral. More research is needed to explain this disagreement.

Deleted: CH_3CO_2H

4. Summary

Gas- and particle-phase measurements were conducted in Yorkville, Georgia (a rural field site) during fall 2016. The goal of the field study was to understand how NH_3 affects particle acidity, and consequently SOA formation through the gas-particle partitioning of semi-volatile inorganic and organic compounds. Since it is a rural site surrounded by forest, agricultural land and CAFOs, this study provided an opportunity for ambient observations in an area impacted by high local emissions of BVOCs and NH_3.

NH_3 concentrations measured by the NH_3-CIMS ranged from 0.7 to 39.0 ppb (average 8.1 ± 5.2 ppb), which were substantially higher than typical levels in the southeastern U.S.. PM_1 inorganic chemical composition, gas-phase HNO_3 and NH_3 concentrations, temperature and RH

were used as model inputs in the ISORROPIA-II thermodynamic model to calculate PM_1 pH and W_i. PM_1 pH ranged from 0.9 to 3.8, with an average pH of 2.2 ± 0.6. The measured and predicted HNO_3-NO_3^- and NH_3-NH_4^+ gas-particle partitioning ratios were in good agreement. The measured gas-phase organic acids were estimated to contribute 30 % of the overall $WSOC_g$ on a carbon mass basis, whereas measured particle-phase organic acids comprised 6 % of the total organic aerosol mass concentration and 4 % of the overall $WSOC_p$ on a carbon mass basis. Formic and acetic acids were the most abundant gas-phase organic acids, with averages of 2.2 ± 1.6 and 1.9 ± 1.3 μg m^{-3}, respectively. Oxalate was the most abundant particle-phase water-soluble organic acid anion, with a average of 0.07 ± 0.05 μg m^{-3}. Measured oxalic acid gas-particle partitioning ratios generally agreed with analytical predictions, which were based on oxalic acid's physicochemical properties (specifically, its Henry's law constants, acid dissociation constants and activity coefficients), temperature, W_i and particle pH. The partitioning of oxalic acid to the particle phase is highly sensitive to temperature and W_i. In contrast, the partitioning of formic and acetic acids to the particle phase were higher than predicted for reasons currently unknown.

Although past air regulations have resulted in decreased sulfate, nitrate and ammonium aerosol mass concentrations across the U.S., our study suggests that the current limited regulation of NH_3 emissions may result in some increase in the organic aerosol mass concentration due to increased gas-to-particle partitioning of some organic acids. However, in this study, the effect was small since the organic acids comprised a small fraction of the overall organic aerosol mass.

5. Acknowledgements

The authors thank Eric Edgerton (Atmospheric Research and Analysis, Inc.) for providing SEARCH network measurements and meteorological data.

6. Funding

This publication was developed under U.S. Environmental Protection Agency (EPA) STAR Grant R835882 awarded to Georgia Institute of Technology. It has not been formally reviewed by the EPA. The views expressed in this document are solely those of the authors and do not necessarily reflect those of the EPA. EPA does not endorse any products or commercial services mentioned in this publication.

7. Competing financial interests

The authors declare no competing financial interests.

8. Data availability

Data can be accessed by request (rweber@eas.gatech.edu).

9. References

Barbier-Jr, J., and Duprez, D.: Steam Effects in 3-way catalysis, Applied Catalysis B-Environmental, 4, 105-140, 10.1016/0926-3373(94)80046-4, 1994.

Bertram, A. K., Martin, S. T., Hanna, S. J., Smith, M. L., Bodsworth, A., Chen, Q., Kuwata, M., Liu, A., You, Y., and Zorn, S. R.: Predicting the relative humidities of liquid-liquid phase separation, efflorescence, and deliquescence of mixed particles of ammonium sulfate, organic material, and water using the organic-to-sulfate mass ratio of the particle and the oxygen-to-carbon elemental ratio of the organic component, Atmos. Chem. Phys., 11, 10995-11006, 10.5194/acp-11-10995-2011, 2011.

Blanchard, C. L., Hidy, G. M., Tanenbaum, S., and Edgerton, E. S.: NMOC, ozone, and organic aerosol in the southeastern United States, 1999-2007: 3. Origins of organic aerosol in Atlanta, Georgia, and surrounding areas, Atmospheric Environment, 45, 1291-1302, 10.1016/j.atmosenv.2010.12.004, 2011.

Blanchard, C. L., Hidy, G. M., Tanenbaum, S., Edgerton, E. S., and Hartsell, B. E.: The Southeastern Aerosol Research and Characterization (SEARCH) study: Spatial variations and chemical climatology, 1999-2010, Journal of the Air & Waste Management Association, 63, 260-275, 10.1080/10962247.2012.749816, 2013a.

Blanchard, C. L., Hidy, G. M., Tanenbaum, S., Edgerton, E. S., and Hartsell, B. E.: The Southeastern Aerosol Research and Characterization (SEARCH) study: Temporal trends in gas and PM concentrations and composition, 1999-2010, Journal of the Air & Waste Management Association, 63, 247-259, 10.1080/10962247.2012.748523, 2013b.

787 Blanchard, C. L., Tanenbaum, S., and Hidy, G. M.: Source Attribution of Air Pollutant
788 Concentrations and Trends in the Southeastern Aerosol Research and Characterization (SEARCH)
789 Network, Environmental Science & Technology, 47, 13536-13545, 10.1021/es402876s, 2013c.

790 Bougiatioti, A., Nikolaou, P., Stavroulas, I., Kouvarakis, G., Weber, R., Nenes, A., Kanakidou,
791 M., and Mihalopoulos, N.: Particle water and pH in the eastern Mediterranean: source variability
792 and implications for nutrient availability, Atmos. Chem. Phys., 16, 4579-4591, 10.5194/acp-16-
793 4579-2016, 2016.

794 Boyd, C. M., Sanchez, J., Xu, L., Eugene, A. J., Nah, T., Tuet, W. Y., Guzman, M. I., and Ng, N.
795 L.: Secondary organic aerosol formation from the beta-pinene+NO3 system: effect of humidity
796 and peroxy radical fate, Atmos. Chem. Phys., 15, 7497-7522, 10.5194/acp-15-7497-2015, 2015.

797 Boyd, C. M., Nah, T., Xu, L., Berkemeier, T., and Ng, N. L.: Secondary Organic Aerosol (SOA)
798 from Nitrate Radical Oxidation of Monoterpenes: Effects of Temperature, Dilution, and Humidity
799 on Aerosol Formation, Mixing, and Evaporation, Environmental Science & Technology, 51, 7831-
800 7841, 10.1021/acs.est.7b01460, 2017.

801 Canagaratna, M. R., Jayne, J. T., Jimenez, J. L., Allan, J. D., Alfarra, M. R., Zhang, Q., Onasch,
802 T. B., Drewnick, F., Coe, H., Middlebrook, A., Delia, A., Williams, L. R., Trimborn, A. M.,
803 Northway, M. J., DeCarlo, P. F., Kolb, C. E., Davidovits, P., and Worsnop, D. R.: Chemical and
804 microphysical characterization of ambient aerosols with the aerodyne aerosol mass spectrometer,
805 Mass Spectrometry Reviews, 26, 185-222, 10.1002/mas.20115, 2007.

806 Canagaratna, M. R., Jimenez, J. L., Kroll, J. H., Chen, Q., Kessler, S. H., Massoli, P., Hildebrandt
807 Ruiz, L., Fortner, E., Williams, L. R., Wilson, K. R., Surratt, J. D., Donahue, N. M., Jayne, J. T.,
808 and Worsnop, D. R.: Elemental ratio measurements of organic compounds using aerosol mass
809 spectrometry: characterization, improved calibration, and implications, Atmos. Chem. Phys., 15,
810 253-272, 10.5194/acp-15-253-2015, 2015.

811 Case, J. L., and Zavodsky, B. T.: Evolution of 2016 drought in the Southeastern United States from
812 a Land surface modeling perspective, Results in Physics, 8, 654-656, 10.1016/j.rinp.2017.12.029,
813 2018.

814 Chen, J. H., Brooks, C. L., and Scheraga, H. A.: Revisiting the carboxylic acid dimers in aqueous
815 solution: Interplay of hydrogen bonding, hydrophobic interactions, and entropy, Journal of
816 Physical Chemistry B, 112, 242-249, 10.1021/jp074355h, 2008.

817 Clegg, S. L., and Brimblecombe, P.: Equilibrium partial pressures and mean activity and osmotic
818 coefficients of 0-100-percent nitric- acid as a function of temperature, Journal of Physical
819 Chemistry, 94, 5369-5380, 10.1021/j100376a038, 1990.

820 Clegg, S. L., Brimblecombe, P., and Khan, L.: The Henry's law constant of oxalic acid and its
821 partitioning into the atmospheric aerosol, Idojaras, 100, 51-68, 1996.

822 Clegg, S. L., Brimblecombe, P., and Wexler, A. S.: Thermodynamic model of the system H+-
823 NH4+-SO42--NO3--H2O at tropospheric temperatures, Journal of Physical Chemistry A, 102,
824 2137-2154, 10.1021/jp973042r, 1998.

825 DeCarlo, P. F., Kimmel, J. R., Trimborn, A., Northway, M. J., Jayne, J. T., Aiken, A. C., Gonin,
826 M., Fuhrer, K., Horvath, T., Docherty, K. S., Worsnop, D. R., and Jimenez, J. L.: Field-deployable,
827 high-resolution, time-of-flight aerosol mass spectrometer, Analytical Chemistry, 78, 8281-8289,
828 10.1021/ac061249n, 2006.

829 Dentener, F. J., and Crutzen, P. J.: A 3-DIMENSIONAL MODEL OF THE GLOBAL AMMONIA
830 CYCLE, Journal of Atmospheric Chemistry, 19, 331-369, 10.1007/bf00694492, 1994.

831 Eatough, D. J., Wadsworth, A., Eatough, D. A., Crawford, J. W., Hansen, L. D., and Lewis, E. A.:
832 A multiple-system, multi-channel diffusion denuder sampler for the determination of fine-
833 particulate organic material in the atmosphere, Atmospheric Environment. Part A. General Topics,
834 27, 1213-1219, 10.1016/0960-1686(93)90247-V, 1993.

835 Edgerton, E. S., Hartsell, B. E., Saylor, R. D., Jansen, J. J., Hansen, D. A., and Hidy, G. M.: The
836 southeastern aerosol research and characterization study: Part II. Filter-based measurements of
837 fine and coarse particulate matter mass and composition, Journal of the Air & Waste Management
838 Association, 55, 1527-1542, 2005.

839 Edgerton, E. S., Hartsell, B. E., Saylor, R. D., Jansen, J. J., Hansen, D. A., and Hidy, G. M.: The
840 Southeastern Aerosol Research and Characterization Study, part 3: Continuous measurements of

841 fine particulate matter mass and composition, Journal of the Air & Waste Management
842 Association, 56, 1325-1341, 10.1080/10473289.2006.10464585, 2006.

843 Edgerton, E. S., Saylor, R. D., Hartsell, B. E., Jansen, J. J., and Hansen, D. A.: Ammonia and
844 ammonium measurements from the southeastern United States, Atmospheric Environment, 41,
845 3339-3351, 10.1016/j.atmosenv.2006.12.034, 2007.

846 Ellis, R. A., Murphy, J. G., Markovic, M. Z., VandenBoer, T. C., Makar, P. A., Brook, J., and
847 Mihele, C.: The influence of gas-particle partitioning and surface-atmosphere exchange on
848 ammonia during BAQS-Met, Atmos. Chem. Phys., 11, 133-145, 10.5194/acp-11-133-2011, 2011.

849 Ellis, R. A., Jacob, D. J., Sulprizio, M. P., Zhang, L., Holmes, C. D., Schichtel, B. A., Blett, T.,
850 Porter, E., Pardo, L. H., and Lynch, J. A.: Present and future nitrogen deposition to national parks
851 in the United States: critical load exceedances, Atmos. Chem. Phys., 13, 9083-9095, 10.5194/acp-
852 13-9083-2013, 2013.

853 Ervens, B., Feingold, G., Frost, G. J., and Kreidenweis, S. M.: A modeling study of aqueous
854 production of dicarboxylic acids: 1. Chemical pathways and speciated organic mass production,
855 Journal of Geophysical Research-Atmospheres, 109, 10.1029/2003jd004387, 2004.

856 Fountoukis, C., and Nenes, A.: ISORROPIA II: a computationally efficient thermodynamic
857 equilibrium model for K+-Ca2+-Mg2+-Nh(4)(+)-Na+-SO42--NO3--Cl--H2O aerosols, Atmos.
858 Chem. Phys., 7, 4639-4659, 2007.

859 Gilson, M. K., Given, J. A., Bush, B. L., and McCammon, J. A.: The statistical-thermodynamic
860 basis for computation of binding affinities: A critical review, Biophysical Journal, 72, 1047-1069,
861 10.1016/s0006-3495(97)78756-3, 1997.

862 Guenther, A. B., Jiang, X., Heald, C. L., Sakulyanontvittaya, T., Duhl, T., Emmons, L. K., and
863 Wang, X.: The Model of Emissions of Gases and Aerosols from Nature version 2.1 (MEGAN2.1):
864 an extended and updated framework for modeling biogenic emissions, Geoscientific Model
865 Development, 5, 1471-1492, 10.5194/gmd-5-1471-2012, 2012.

866 Guo, H., Xu, L., Bougiatioti, A., Cerully, K. M., Capps, S. L., Hite, J. R., Jr., Carlton, A. G., Lee,
867 S. H., Bergin, M. H., Ng, N. L., Nenes, A., and Weber, R. J.: Fine-particle water and pH in the

868 southeastern United States, Atmos. Chem. Phys., 15, 5211-5228, 10.5194/acp-15-5211-2015,
869 2015.

870 Guo, H., Sullivan, A. P., Campuzano-Jost, P., Schroder, J. C., Lopez-Hilfiker, F. D., Dibb, J. E.,
871 Jimenez, J. L., Thornton, J. A., Brown, S. S., Nenes, A., and Weber, R. J.: Fine particle pH and
872 the partitioning of nitric acid during winter in the northeastern United States, Journal of
873 Geophysical Research-Atmospheres, 121, 10355-10376, 10.1002/2016jd025311, 2016.

874 Guo, H., Liu, J. M., Froyd, K. D., Roberts, J. M., Veres, P. R., Hayes, P. L., Jimenez, J. L., Nenes,
875 A., and Weber, R. J.: Fine particle pH and gas-particle phase partitioning of inorganic species in
876 Pasadena, California, during the 2010 CalNex campaign, Atmos. Chem. Phys., 17, 5703-5719,
877 10.5194/acp-17-5703-2017, 2017a.

878 Guo, H., Nenes, A., and Weber, R. J.: The underappreciated role of nonvolatile cations on aerosol
879 ammonium-sulfate molar ratios, Atmos. Chem. Phys. Discuss., 2017, 1-19, 10.5194/acp-2017-
880 737, 2017b.

881 Guo, H., Weber, R. J., and Nenes, A.: High levels of ammonia do not raise fine particle pH
882 sufficiently to yield nitrogen oxide-dominated sulfate production, Scientific Reports, 7,
883 10.1038/s41598-017-11704-0, 2017c.

884 Hansen, D. A., Edgerton, E. S., Hartsell, B. E., Jansen, J. J., Kandasamy, N., Hidy, G. M., and
885 Blanchard, C. L.: The southeastern aerosol research and characterization study: Part 1-overview,
886 Journal of the Air & Waste Management Association, 53, 1460-1471, 2003.

887 Haynes, W. M.: CRC handbook of chemistry and physics: A ready-reference book of chemical
888 and physical data. , Boca Raton: CRC Press, 2014.

889 Hennigan, C. J., Izumi, J., Sullivan, A. P., Weber, R. J., and Nenes, A.: A critical evaluation of
890 proxy methods used to estimate the acidity of atmospheric particles, Atmos. Chem. Phys., 15,
891 2775-2790, 10.5194/acp-15-2775-2015, 2015.

892 Huey, L. G., Hanson, D. R., and Howard, C. J.: Reactions of SF6- and I- with Atmospheric Trace
893 Gases, Journal of Physical Chemistry, 99, 5001-5008, 10.1021/j100014a021, 1995.

894 Huey, L. G., Tanner, D. J., Slusher, D. L., Dibb, J. E., Arimoto, R., Chen, G., Davis, D., Buhr, M.
895 P., Nowak, J. B., Mauldin, R. L., Eisele, F. L., and Kosciuch, E.: CIMS measurements of HNO3
896 and SO2 at the South Pole during ISCAT 2000, Atmospheric Environment, 38, 5411-5421,
897 10.1016/j.atmosenv.2004.04.037, 2004.

898 Kawamura, K., and Gagosian, R. B.: Implication of omega-oxocarboxylic acids in the remote
899 marine atmosphere for photo-oxidation of unsaturated fatty acids, Nature, 325, 330-332,
900 10.1038/325330a0, 1987.

901 Kawamura, K., and Ikushima, K.: Seasonal changes in the distribution of dicarboxylic acids in the
902 urban atmosphere, Environmental Science & Technology, 27, 2227-2235, 10.1021/es00047a033,
903 1993.

904 Kawamura, K., and Bikkina, S.: A review of dicarboxylic acids and related compounds in
905 atmospheric aerosols: Molecular distributions, sources and transformation, Atmospheric Research,
906 170, 140-160, 10.1016/j.atmosres.2015.11.018, 2016.

907 Kerminen, V. M., Ojanen, C., Pakkanen, T., Hillamo, R., Aurela, M., and Merilainen, J.: Low-
908 molecular-weight dicarboxylic acids in an urban and rural atmosphere, Journal of Aerosol Science,
909 31, 349-362, 10.1016/s0021-8502(99)00063-4, 2000.

910 Lamarque, J. F., Bond, T. C., Eyring, V., Granier, C., Heil, A., Klimont, Z., Lee, D., Liousse, C.,
911 Mieville, A., Owen, B., Schultz, M. G., Shindell, D., Smith, S. J., Stehfest, E., Van Aardenne, J.,
912 Cooper, O. R., Kainuma, M., Mahowald, N., McConnell, J. R., Naik, V., Riahi, K., and van
913 Vuuren, D. P.: Historical (1850-2000) gridded anthropogenic and biomass burning emissions of
914 reactive gases and aerosols: methodology and application, Atmos. Chem. Phys., 10, 7017-7039,
915 10.5194/acp-10-7017-2010, 2010.

916 Laskin, A., Laskin, J., and Nizkorodov, S. A.: Chemistry of Atmospheric Brown Carbon, Chemical
917 Reviews, 115, 4335-4382, 10.1021/cr5006167, 2015.

918 Laskin, J., Laskin, A., Roach, P. J., Slysz, G. W., Anderson, G. A., Nizkorodov, S. A., Bones, D.
919 L., and Nguyen, L. Q.: High-Resolution Desorption Electrospray Ionization Mass Spectrometry

for Chemical Characterization of Organic Aerosols, Analytical Chemistry, 82, 2048-2058, 10.1021/ac902801f, 2010.

Lee, B. H., Mohr, C., Lopez-Hilfiker, F. D., Lutz, A., Hallquist, M., Lee, L., Romer, P., Cohen, R. C., Iyer, S., Kurten, T., Hu, W. W., Day, D. A., Campuzano-Jost, P., Jimenez, J. L., Xu, L., Ng, N. L., Guo, H. Y., Weber, R. J., Wild, R. J., Brown, S. S., Koss, A., de Gouw, J., Olson, K., Goldstein, A. H., Seco, R., Kim, S., McAvey, K., Shepson, P. B., Starn, T., Baumann, K., Edgerton, E. S., Liu, J. M., Shilling, J. E., Miller, D. O., Brune, W., Schobesberger, S., D'Ambro, E. L., and Thornton, J. A.: Highly functionalized organic nitrates in the southeast United States: Contribution to secondary organic aerosol and reactive nitrogen budgets, Proceedings of the National Academy of Sciences of the United States of America, 113, 1516-1521, 10.1073/pnas.1508108113, 2016.

Lee, B. P., Li, Y. J., Yu, J. Z., Louie, P. K. K., and Chan, C. K.: Characteristics of submicron particulate matter at the urban roadside in downtown Hong Kong-Overview of 4 months of continuous high-resolution aerosol mass spectrometer measurements, Journal of Geophysical Research-Atmospheres, 120, 7040-7058, 10.1002/2015jd023311, 2015.

Lee, H. J., Laskin, A., Laskin, J., and Nizkorodov, S. A.: Excitation-Emission Spectra and Fluorescence Quantum Yields for Fresh and Aged Biogenic Secondary Organic Aerosols, Environmental Science & Technology, 47, 5763-5770, 10.1021/es400644c, 2013.

Lim, H. J., Carlton, A. G., and Turpin, B. J.: Isoprene forms secondary organic aerosol through cloud processing: Model simulations, Environmental Science & Technology, 39, 4441-4446, 10.1021/es048039h, 2005.

Liu, J., Zhang, X., Parker, E. T., Veres, P. R., Roberts, J. M., de Gouw, J. A., Hayes, P. L., Jimenez, J. L., Murphy, J. G., Ellis, R. A., Huey, L. G., and Weber, R. J.: On the gas-particle partitioning of soluble organic aerosol in two urban atmospheres with contrasting emissions: 2. Gas and particle phase formic acid, Journal of Geophysical Research-Atmospheres, 117, 10.1029/2012jd017912, 2012.

946 Livingston, C., Rieger, P., and Winer, A.: Ammonia emissions from a representative in-use fleet
947 of light and medium-duty vehicles in the California South Coast Air Basin, Atmospheric
948 Environment, 43, 3326-3333, 10.1016/j.atmosenv.2009.04.009, 2009.

949 Malm, W. C., and Day, D. E.: Estimates of aerosol species scattering characteristics as a function
950 of relative humidity, Atmospheric Environment, 35, 2845-2860, 10.1016/s1352-2310(01)00077-
951 2, 2001.

952 Middlebrook, A. M., Bahreini, R., Jimenez, J. L., and Canagaratna, M. R.: Evaluation of
953 Composition-Dependent Collection Efficiencies for the Aerodyne Aerosol Mass Spectrometer
954 using Field Data, Aerosol Science and Technology, 46, 258-271, 10.1080/02786826.2011.620041,
955 2012.

956 Na, K., Song, C., Switzer, C., and Cocker, D. R.: Effect of ammonia on secondary organic aerosol
957 formation from alpha-Pinene ozonolysis in dry and humid conditions, Environmental Science &
958 Technology, 41, 6096-6102, 10.1021/es061956y, 2007.

959 Nah, T., Ji, Y., Tanner, D. J., Guo, H., Sullivan, A. P., Ng, N. L., Weber, R. J., and Huey, L. G.:
960 Real-time measurements of gas-phase organic acids using SF6- chemical ionization mass
961 spectrometry, Atmos. Meas. Tech. Discuss., 2018, 1-40, 10.5194/amt-2018-46, 2018.

962 Nenes, A., Pandis, S. N., and Pilinis, C.: ISORROPIA: A new thermodynamic equilibrium model
963 for multiphase multicomponent inorganic aerosols, Aquatic Geochemistry, 4, 123-152,
964 10.1023/a:1009604003981, 1998.

965 Neuman, J. A., Ryerson, T. B., Huey, L. G., Jakoubek, R., Nowak, J. B., Simons, C., and
966 Fehsenfeld, F. C.: Calibration and evaluation of nitric acid and ammonia permeation tubes by UV
967 optical absorption, Environmental Science & Technology, 37, 2975-2981, 10.1021/es0264221,
968 2003.

969 Ng, N. L., Brown, S. S., Archibald, A. T., Atlas, E., Cohen, R. C., Crowley, J. N., Day, D. A.,
970 Donahue, N. M., Fry, J. L., Fuchs, H., Griffin, R. J., Guzman, M. I., Herrmann, H., Hodzic, A.,
971 Iinuma, Y., Jimenez, J. L., Kiendler-Scharr, A., Lee, B. H., Luecken, D. J., Mao, J. Q., McLaren,
972 R., Mutzel, A., Osthoff, H. D., Ouyang, B., Picquet-Varrault, B., Platt, U., Pye, H. O. T., Rudich,

973 Y., Schwantes, R. H., Shiraiwa, M., Stutz, J., Thornton, J. A., Tilgner, A., Williams, B. J., and
974 Zaveri, R. A.: Nitrate radicals and biogenic volatile organic compounds: oxidation, mechanisms,
975 and organic aerosol, Atmos. Chem. Phys., 17, 2103-2162, 10.5194/acp-17-2103-2017, 2017.

976 Nowak, J. B., Huey, L. G., Eisele, F. L., Tanner, D. J., Mauldin, R. L., Cantrell, C., Kosciuch, E.,
977 and Davis, D. D.: Chemical ionization mass spectrometry technique for detection of
978 dimethylsulfoxide and ammonia, Journal of Geophysical Research-Atmospheres, 107,
979 10.1029/2001jd001058, 2002.

980 Nowak, J. B., Huey, L. G., Russell, A. G., Tian, D., Neuman, J. A., Orsini, D., Sjostedt, S. J.,
981 Sullivan, A. P., Tanner, D. J., Weber, R. J., Nenes, A., Edgerton, E., and Fehsenfeld, F. C.:
982 Analysis of urban gas phase ammonia measurements from the 2002 Atlanta Aerosol Nucleation
983 and Real-Time Characterization Experiment (ANARChE), Journal of Geophysical Research-
984 Atmospheres, 111, 14, 10.1029/2006jd007113, 2006.

985 Orsini, D. A., Ma, Y. L., Sullivan, A., Sierau, B., Baumann, K., and Weber, R. J.: Refinements to
986 the particle-into-liquid sampler (PILS) for ground and airborne measurements of water soluble
987 aerosol composition, Atmospheric Environment, 37, 1243-1259, 10.1016/s1352-2310(02)01015-
988 4, 2003.

989 Park Williams, A., Cook, B. I., Smerdon, J. E., Bishop, D. A., Seager, R., and Mankin, J. S.: The
990 2016 Southeastern U.S. Drought: An Extreme Departure From Centennial Wetting and Cooling,
991 Journal of Geophysical Research: Atmospheres, 122, 10,888-810,905, 10.1002/2017JD027523,
992 2017.

993 Pechony, O., and Shindell, D. T.: Driving forces of global wildfires over the past millennium and
994 the forthcoming century, Proceedings of the National Academy of Sciences of the United States
995 of America, 107, 19167-19170, 10.1073/pnas.1003669107, 2010.

996 Pye, H. O. T., Luecken, D. J., Xu, L., Boyd, C. M., Ng, N. L., Baker, K. R., Ayres, B. R., Bash, J.
997 O., Baumann, K., Carter, W. P. L., Edgerton, E., Fry, J. L., Hutzell, W. T., Schwede, D. B., and
998 Shepson, P. B.: Modeling the Current and Future Roles of Particulate Organic Nitrates in the
999 Southeastern United States, Environmental Science & Technology, 49, 14195-14203,
1000 10.1021/acs.est.5b03738, 2015.

Reis, S., Pinder, R. W., Zhang, M., Lijie, G., and Sutton, M. A.: Reactive nitrogen in atmospheric emission inventories, Atmos. Chem. Phys., 9, 7657-7677, 10.5194/acp-9-7657-2009, 2009.

Sander, R.: Compilation of Henry's law constants (version 4.0) for water as solvent, Atmos. Chem. Phys., 15, 4399-4981, 10.5194/acp-15-4399-2015, 2015.

Saxena, P., and Hildemann, L. M.: Water-soluble organics in atmospheric particles: A critical review of the literature and application of thermodynamics to identify candidate compounds, Journal of Atmospheric Chemistry, 24, 57-109, 10.1007/bf00053823, 1996.

Saylor, R., Myles, L., Sibble, D., Caldwell, J., and Xing, J.: Recent trends in gas-phase ammonia and PM2.5 ammonium in the Southeast United States, Journal of the Air & Waste Management Association, 65, 347-357, 10.1080/10962247.2014.992554, 2015.

Schrier, E. E., Pottle, M., and Scheraga, H. A.: The Influence of Hydrogen and Hydrophobic Bonds on the Stability of the Carboxylic Acid Dimers in Aqueous Solution, Journal of the American Chemical Society, 86, 3444-3449, 10.1021/ja01071a009, 1964.

Seinfeld, J. H., and Pandis, S. N.: Atmospheric chemistry and physics : from air pollution to climate change, Third edition. ed., John Wiley & Sons, Inc., Hoboken, New Jersey, xxvi, 1120 pages pp., 2016.

Shi, G. L., Xu, J., Peng, X., Xiao, Z. M., Chen, K., Tian, Y. Z., Guan, X. B., Feng, Y. C., Yu, H. F., Nenes, A., and Russell, A. G.: pH of Aerosols in a Polluted Atmosphere: Source Contributions to Highly Acidic Aerosol, Environmental Science & Technology, 51, 4289-4296, 10.1021/acs.est.6b05736, 2017.

Song, M., Marcolli, C., Krieger, U. K., Zuend, A., and Peter, T.: Liquid-liquid phase separation and morphology of internally mixed dicarboxylic acids/ammonium sulfate/water particles, Atmos. Chem. Phys., 12, 2691-2712, 10.5194/acp-12-2691-2012, 2012.

Song, S., Gao, M., Xu, W., Shao, J., Shi, G., Wang, S., Wang, Y., Sun, Y., and McElroy, M. B.: Fine particle pH for Beijing winter haze as inferred from different thermodynamic equilibrium models, Atmos. Chem. Phys. Discuss., 2018, 1-26, 10.5194/acp-2018-6, 2018.

1027 Sorooshian, A., Ng, N. L., Chan, A. W. H., Feingold, G., Flagan, R. C., and Seinfeld, J. H.:
1028 Particulate organic acids and overall water-soluble aerosol composition measurements from the
1029 2006 Gulf of Mexico Atmospheric Composition and Climate Study (GoMACCS), Journal of
1030 Geophysical Research-Atmospheres, 112, 16, 10.1029/2007jd008537, 2007.

1031 Sorooshian, A., Murphy, S. M., Hersey, S., Bahreini, R., Jonsson, H., Flagan, R. C., and Seinfeld,
1032 J. H.: Constraining the contribution of organic acids and AMS m/z 44 to the organic aerosol
1033 budget: On the importance of meteorology, aerosol hygroscopicity, and region, Geophys. Res.
1034 Lett., 37, 5, 10.1029/2010gl044951, 2010.

1035 Spaulding, R. S., Talbot, R. W., and Charles, M. J.: Optimization of a mist chamber (cofer
1036 scrubber) for sampling water-soluble organics in air, Environmental Science & Technology, 36,
1037 1798-1808, 10.1021/es011189x, 2002.

1038 Suarez-Bertoa, R., Zardini, A. A., and Astorga, C.: Ammonia exhaust emissions from spark
1039 ignition vehicles over the New European Driving Cycle, Atmospheric Environment, 97, 43-53,
1040 10.1016/j.atmosenv.2014.07.050, 2014.

1041 Sullivan, A. P., Weber, R. J., Clements, A. L., Turner, J. R., Bae, M. S., and Schauer, J. J.: A
1042 method for on-line measurement of water-soluble organic carbon in ambient aerosol particles:
1043 Results from an urban site, Geophysical Research Letters, 31, 10.1029/2004gl019681, 2004.

1044 Sun, K., Tao, L., Miller, D. J., Pan, D., Golston, L. M., Zondlo, M. A., Griffin, R. J., Wallace, H.
1045 W., Leong, Y. J., Yang, M. M., Zhang, Y., Mauzerall, D. L., and Zhu, T.: Vehicle Emissions as an
1046 Important Urban Ammonia Source in the United States and China, Environmental Science &
1047 Technology, 51, 2472-2481, 10.1021/acs.est.6b02805, 2017.

1048 Updyke, K. M., Nguyen, T. B., and Nizkorodov, S. A.: Formation of brown carbon via reactions
1049 of ammonia with secondary organic aerosols from biogenic and anthropogenic precursors,
1050 Atmospheric Environment, 63, 22-31, 10.1016/j.atmosenv.2012.09.012, 2012.

1051 Van Damme, M., Clarisse, L., Heald, C. L., Hurtmans, D., Ngadi, Y., Clerbaux, C., Dolman, A.
1052 J., Erisman, J. W., and Coheur, P. F.: Global distributions, time series and error characterization

of atmospheric ammonia (NH3) from IASI satellite observations, Atmos. Chem. Phys., 14, 2905-2922, 10.5194/acp-14-2905-2014, 2014.

Warner, J. X., Wei, Z. G., Strow, L. L., Dickerson, R. R., and Nowak, J. B.: The global tropospheric ammonia distribution as seen in the 13-year AIRS measurement record, Atmos. Chem. Phys., 16, 5467-5479, 10.5194/acp-16-5467-2016, 2016.

Warner, J. X., Dickerson, R. R., Wei, Z., Strow, L. L., Wang, Y., and Liang, Q.: Increased atmospheric ammonia over the world's major agricultural areas detected from space, Geophysical Research Letters, 44, 2875-2884, 10.1002/2016gl072305, 2017.

Weber, R. J., Orsini, D., Daun, Y., Lee, Y. N., Klotz, P. J., and Brechtel, F.: A particle-into-liquid collector for rapid measurement of aerosol bulk chemical composition, Aerosol Science and Technology, 35, 718-727, 10.1080/02786820152546761, 2001.

Weber, R. J., Lee, S., Chen, G., Wang, B., Kapustin, V., Moore, K., Clarke, A. D., Mauldin, L., Kosciuch, E., Cantrell, C., Eisele, F., Thornton, D. C., Bandy, A. R., Sachse, G. W., and Fuelberg, H. E.: New particle formation in anthropogenic plumes advecting from Asia observed during TRACE-P, Journal of Geophysical Research-Atmospheres, 108, 13, 10.1029/2002jd003112, 2003.

Weber, R. J., Guo, H., Russell, A. G., and Nenes, A.: High aerosol acidity despite declining atmospheric sulfate concentrations over the past 15 years, Nature Geoscience, 9, 282-+, 10.1038/ngeo2665, 2016.

Whittington, B. I., Jiang, C. J., and Trimm, D. L.: Vehicle exhaust catalysis: I. The relative importance of catalytic oxidation, steam reforming and water-gas shift reactions, Catalysis Today, 26, 41-45, 10.1016/0920-5861(95)00093-u, 1995.

Xing, J., Pleim, J., Mathur, R., Pouliot, G., Hogrefe, C., Gan, C. M., and Wei, C.: Historical gaseous and primary aerosol emissions in the United States from 1990 to 2010, Atmos. Chem. Phys., 13, 7531-7549, 10.5194/acp-13-7531-2013, 2013.

Xu, L., Guo, H., Boyd, C. M., Klein, M., Bougiatioti, A., Cerully, K. M., Hite, J. R., Isaacman-VanWertz, G., Kreisberg, N. M., Knote, C., Olson, K., Koss, A., Goldstein, A. H., Hering, S. V.,

de Gouw, J., Baumann, K., Lee, S.-H., Nenes, A., Weber, R. J., and Ng, N. L.: Effects of anthropogenic emissions on aerosol formation from isoprene and monoterpenes in the southeastern United States, Proceedings of the National Academy of Sciences of the United States of America, 112, 37-42, 10.1073/pnas.1417609112, 2015a.

Xu, L., Suresh, S., Guo, H., Weber, R. J., and Ng, N. L.: Aerosol characterization over the southeastern United States using high-resolution aerosol mass spectrometry: spatial and seasonal variation of aerosol composition and sources with a focus on organic nitrates, Atmos. Chem. Phys., 15, 7307-7336, 10.5194/acp-15-7307-2015, 2015b.

Xu, L., Guo, H. Y., Weber, R. J., and Ng, N. L.: Chemical Characterization of Water-Soluble Organic Aerosol in Contrasting Rural and Urban Environments in the Southeastern United States, Environmental Science & Technology, 51, 78-88, 10.1021/acs.est.6b05002, 2017.

Yao, X. H., Hu, Q. J., Zhang, L. M., Evans, G. J., Godri, K. J., and Ng, A. C.: Is vehicular emission a significant contributor to ammonia in the urban atmosphere?, Atmospheric Environment, 80, 499-506, 10.1016/j.atmosenv.2013.08.028, 2013.

You, Y., Renbaum-Wolff, L., and Bertram, A. K.: Liquid-liquid phase separation in particles containing organics mixed with ammonium sulfate, ammonium bisulfate, ammonium nitrate or sodium chloride, Atmos. Chem. Phys., 13, 11723-11734, 10.5194/acp-13-11723-2013, 2013.

You, Y., Kanawade, V. P., de Gouw, J. A., Guenther, A. B., Madronich, S., Sierra-Hernandez, M. R., Lawler, M., Smith, J. N., Takahama, S., Ruggeri, G., Koss, A., Olson, K., Baumann, K., Weber, R. J., Nenes, A., Guo, H., Edgerton, E. S., Porcelli, L., Brune, W. H., Goldstein, A. H., and Lee, S. H.: Atmospheric amines and ammonia measured with a chemical ionization mass spectrometer (CIMS), Atmos. Chem. Phys., 14, 12181-12194, 10.5194/acp-14-12181-2014, 2014a.

You, Y., Smith, M. L., Song, M., Martin, S. T., and Bertram, A. K.: Liquid-liquid phase separation in atmospherically relevant particles consisting of organic species and inorganic salts, International Reviews in Physical Chemistry, 33, 43-77, 10.1080/0144235x.2014.890786, 2014b.

1105 You, Y., and Bertram, A. K.: Effects of molecular weight and temperature on liquid-liquid phase
1106 separation in particles containing organic species and inorganic salts, Atmos. Chem. Phys., 15,
1107 1351-1365, 10.5194/acp-15-1351-2015, 2015.

1108 Yu, H., and Lee, S. H.: Chemical ionisation mass spectrometry for the measurement of
1109 atmospheric amines, Environ. Chem., 9, 190-201, 10.1071/en12020, 2012.

1110 Zhang, H. F., Yee, L. D., Lee, B. H., Curtis, M. P., Worton, D. R., Isaacman-VanWertz, G.,
1111 Offenberg, J. H., Lewandowski, M., Kleindienst, T. E., Beaver, M. R., Holder, A. L., Lonneman,
1112 W. A., Docherty, K. S., Jaoui, M., Pye, H. O. T., Hu, W. W., Day, D. A., Campuzano-Jost, P.,
1113 Jimenez, J. L., Guo, H. Y., Weber, R. J., de Gouw, J., Koss, A. R., Edgerton, E. S., Brune, W.,
1114 Mohr, C., Lopez-Hilfiker, F. D., Lutz, A., Kreisberg, N. M., Spielman, S. R., Hering, S. V., Wilson,
1115 K. R., Thornton, J. A., and Goldstein, A. H.: Monoterpenes are the largest source of summertime
1116 organic aerosol in the southeastern United States, Proceedings of the National Academy of
1117 Sciences of the United States of America, 115, 2038-2043, 10.1073/pnas.1717513115, 2018.

1118 Zuend, A., Marcolli, C., Luo, B. P., and Peter, T.: A thermodynamic model of mixed organic-
1119 inorganic aerosols to predict activity coefficients, Atmos. Chem. Phys., 8, 4559-4593,
1120 10.5194/acp-8-4559-2008, 2008.

1121 Zuend, A., Marcolli, C., Booth, A. M., Lienhard, D. M., Soonsin, V., Krieger, U. K., Topping, D.
1122 O., McFiggans, G., Peter, T., and Seinfeld, J. H.: New and extended parameterization of the
1123 thermodynamic model AIOMFAC: calculation of activity coefficients for organic-inorganic
1124 mixtures containing carboxyl, hydroxyl, carbonyl, ether, ester, alkenyl, alkyl, and aromatic
1125 functional groups, Atmos. Chem. Phys., 11, 9155-9206, 10.5194/acp-11-9155-2011, 2011.

1126 Zuend, A., Marcolli, C., Luo, B. P., and Peter, T.: A thermodynamic model of mixed organic-
1127 inorganic aerosols to predict activity coefficients (vol 8, pg 4559, 2008), Atmos. Chem. Phys., 12,
1128 10075-10075, 10.5194/acp-12-10075-2012, 2012.
1129

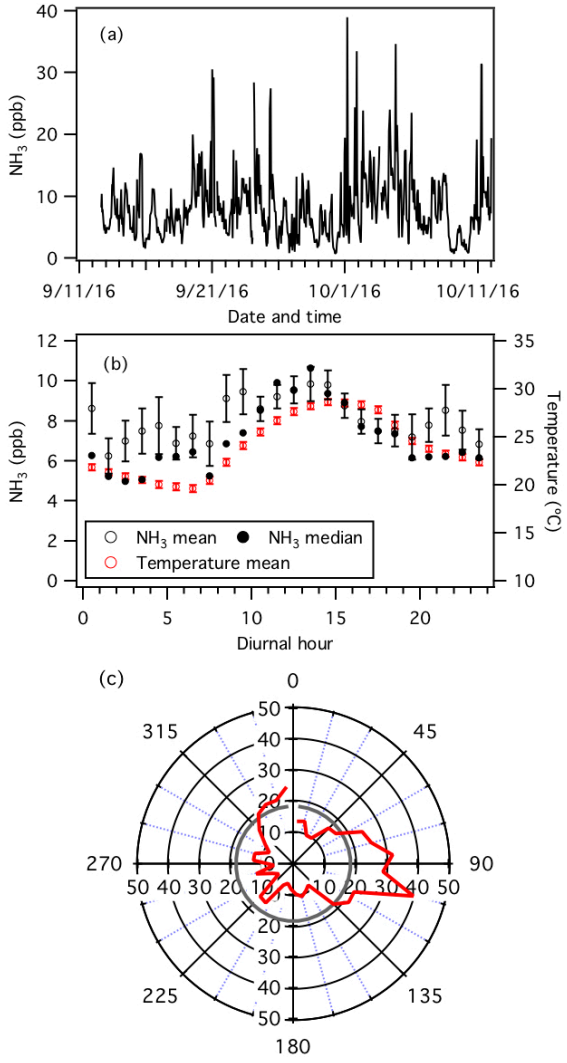

1130

1131 **Figure 1:** Measurements by the NH_3-CIMS during the second half of the study. (a) Time series of
1132 NH_3 concentration. The data is displayed as 1-hour averages. (b) Diurnal profiles of NH_3
1133 concentration (mean and median) and temperature. Error bars shown are the standard errors. Dates
1134 and times displayed are local time. All the concentrations represent averages in 1-hour intervals

1135 and the standard errors are plotted as error bars. (c) Average NH_3 concentration normalized to
1136 wind speed (i.e., NH_3 concentration (ppb) x wind speed (m s^{-1})) in each 10 degrees bin (red line).
1137 The average normalized NH_3 concentration is shown as a grey line.

1138

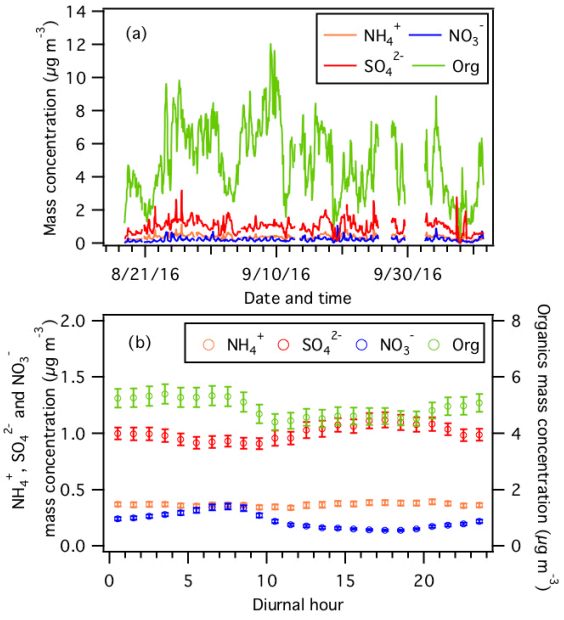

1139

1140 **Figure 2:** (a) Time series and (b) diurnal profiles of non-refractory PM_1 species measured by the
1141 AMS. Error bars shown in panel (b) are the standard errors. Dates and times displayed are local
1142 time.

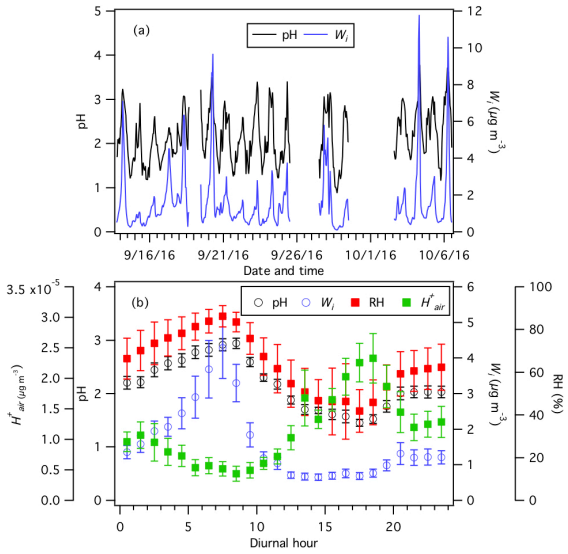

1143

1144 **Figure 3:** (a) Time series and (b) diurnal profiles of ISORROPIA-predicted PM_1 pH and W_i. The
1145 diurnal profiles of RH and ISORROPIA-predicted H^+_{air} are also shown in panel (b). Dates and
1146 times displayed are local time. All the data shown here represent averages in 1-hour intervals.
1147 Error bars shown in panel (b) are the standard errors.

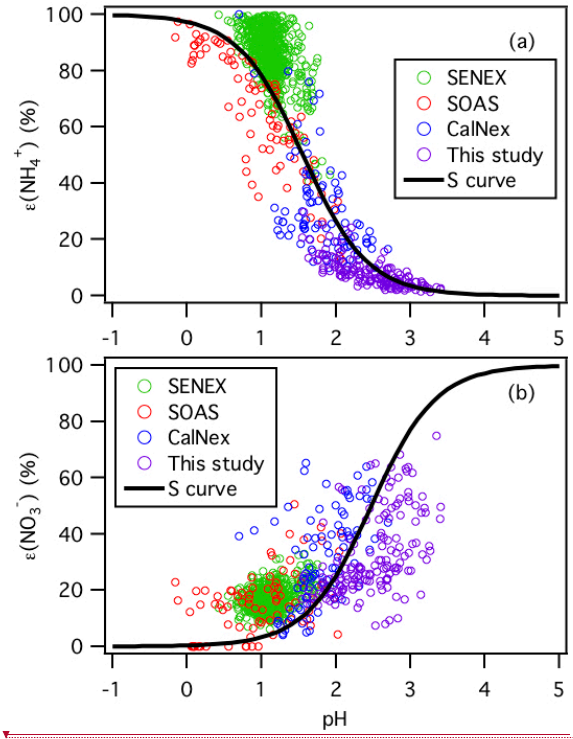

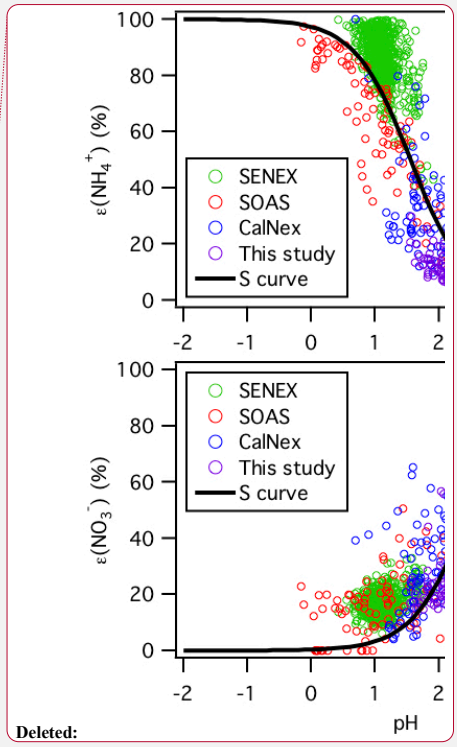

Deleted:

Figure 4: Analytically calculated S curves of $\varepsilon(NH_4^+)$ and $\varepsilon(NO_3^-)$ and ambient data plotted against ISORROPIA-predicted particle pH for this study, SENEX, SOAS and CalNex. For the ambient datasets, a narrow range of W_i (1 to 4 μg m^{-3}) and temperature (15 to 25 °C) are selected to be close to the analytical calculation input (i.e., W_i = 2.5 μg m^{-3} and temperature = 20 °C). Similar to Guo et al. (2017a), $\gamma_{NH_4^+} = 1$ and $\gamma_{H^+-NO_3^-} = \sqrt{\gamma_{H^+}\gamma_{NO_3^-}} = 0.28$ are used for the analytically calculated S curves.

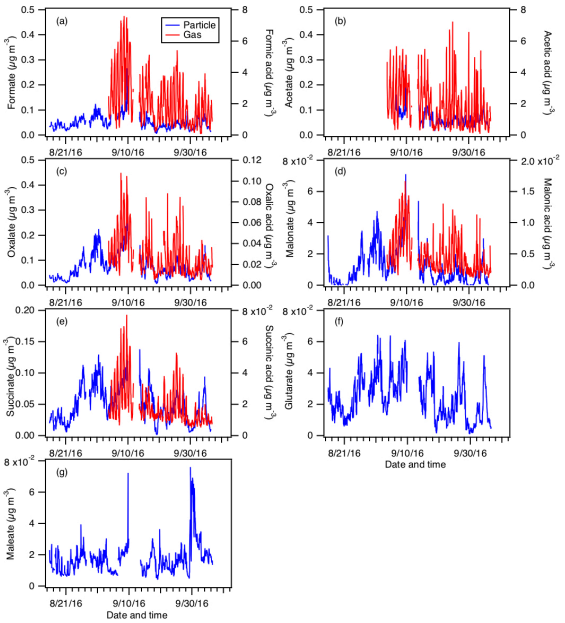

Figure 5: Particle- and gas-phase measurements of (a) formic, (b) acetic, (c) oxalic, (d) malonic, (e) succinic, (f) glutaric, and (g) maleic acids. Particle-phase measurements are shown on the left y axes, while gas-phase measurements are shown on the right y axes. Dates and times displayed are local time. Gas-phase measurements of glutaric and maleic acids are not available.

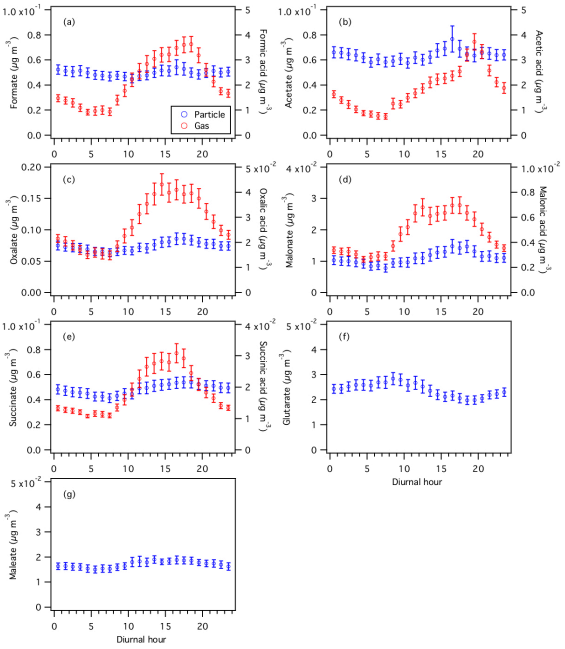

Figure 6: Diurnal profiles of particle- and gas-phase (a) formic, (b) acetic, (c) oxalic, (d) malonic, (e) succinic, (f) glutaric, and (g) maleic acids. Particle-phase measurements are shown on the left y axes, while gas-phase measurements are shown on the right y axes. All the data shown here represent averages in 1-hour intervals. Error bars shown are the standard errors.

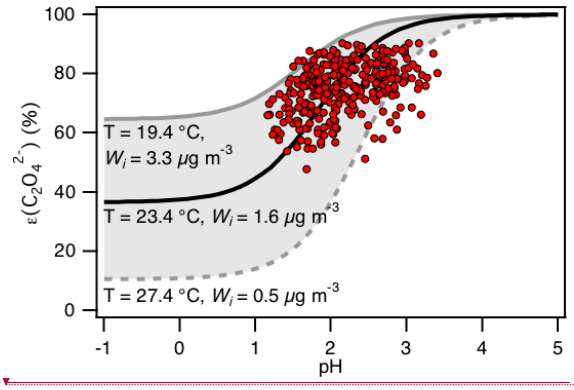

Deleted:

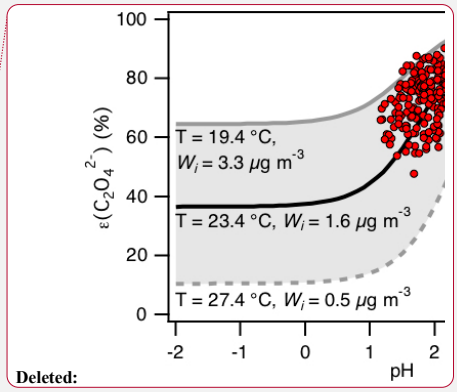

Figure 7: Analytically calculated S curve of $\varepsilon(C_2O_4^{2-})$ and ambient data from 13 September to 6 October 2016 plotted against ISORROPIA-predicted particle pH. For the ambient data, a range in W_i (0.5 to 4 μg m^{-3}) and temperature (15 to 31 °C) are chosen to be close to the analytically calculated outputs. For the analytically calculated S curves, we used $\gamma_{C_2H_2O_4} = 0.0492$ (AIOMFAC predicted). We also assumed that $\gamma_{H^+}\gamma_{C_2HO_4^-} = \gamma_{H^+}\gamma_{NO_3^-}$, and used the ISORROPIA-predicted $\gamma_{H^+-NO_3^-} = \sqrt{\gamma_{H^+}\gamma_{NO_3^-}} = 0.265$. The black line is the S curve calculated using the selected time period's average temperature (23.4 ± 4.0 °C) and W_i (1.6 ± 1.7 μg m^{-3}). The grey lines are S curves calculated using one standard deviation from the average temperature and W_i (i.e., temperature = 27.4 °C and W_i = 0.5 μg m^{-3} for dotted grey line, temperature = 19.4 °C and W_i = 3.3 μg m^{-3} for solid grey line).

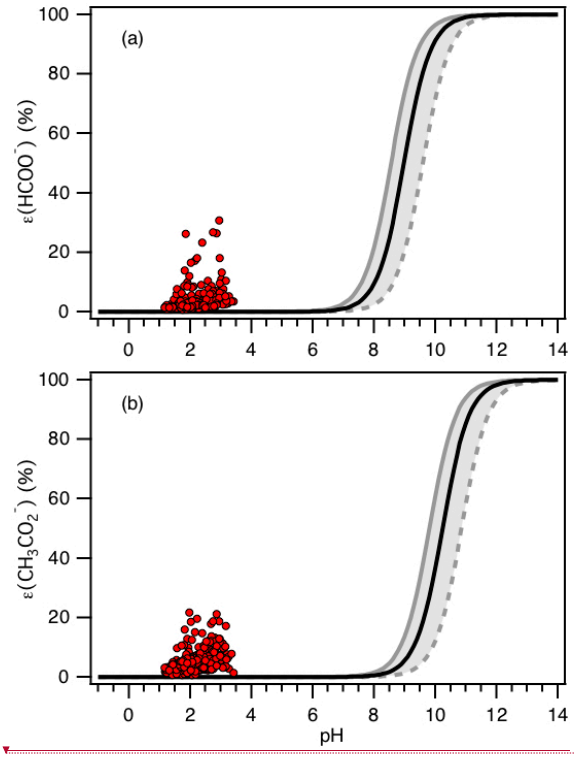

Deleted:

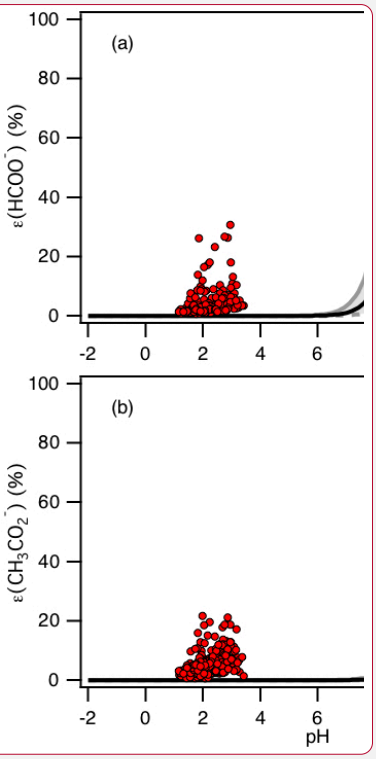

Figure 8: Analytically calculated S curves of ε($HCOO^-$) and ε($CH_3CO_2^-$) (solid black lines) and ambient data from 13 September to 6 October 2016 plotted against ISORROPIA-predicted particle pH (shown in panels (a) and (b), respectively). For the ambient data, a narrow range in W_i (0.5 to 4 μg m^{-3}) and RH (20 to 90 %) is chosen to be close to the analytically calculated outputs. For the analytically calculated S curves, we used γ_{HCOOH} = 0.334 and γ_{CH_3COOH} = 2.150 (AIOMFAC predicted). We also assumed that $\gamma_{H^+}\gamma_{HCOO^-} = \gamma_{H^+}\gamma_{CH_3COO^-} = \gamma_{H^+}\gamma_{NO_3^-}$, and used the ISORROPIA-predicted $\gamma_{H^+-NO_3^-} = \sqrt{\gamma_{H^+}\gamma_{NO_3^-}}$ = 0.265. The black lines are S curves calculated using the selected time period's average temperature (23.4 ± 4.0 °C) and W_i (1.6 ± 1.7 μg m^{-3}). The grey lines are S curves calculated using one standard deviation from the average temperature and W_i (i.e., temperature = 27.4 °C and W_i = 0.5 μg m^{-3} for dotted grey line, temperature = 19.4 °C and W_i = 3.3 μg m^{-3} for solid grey line).

Table 1: Comparisons between different field campaigns for particle pH, major inorganic ions and gases and meteorological conditions. All pH values were calculated using ISORROPIA-II run in forward mode. These statistics were previously compiled by Guo et al. (2017a). Campaign acronyms used here stand for the California Research at the Nexus of Air Quality and Climate Change (CalNex), Southern Oxidant and Aerosol Study (SOAS), and Southeastern Nexus of Air Quality and Climate (SENEX).

Campaign	CalNex		SOAS	SENEX	This study
Type	Ground		Ground	Aircraft	Ground
PM cut size	PM_1	$PM_{2.5}$[a]	PM_1&$PM_{2.5}$[b]	PM_1	PM_1
Year	2010		2013	2013	2016
Season	(Early Summer)		Summer	Summer	Fall
Region/Location	SW US		SE US	SE US	SE US
SO_4^{2-}, μg m^{-3}	2.86 ± 1.70	1.88 ± 0.69	1.73 ± 1.21	2.05 ± 0.80	1.6 ± 0.4
NO_3^-, μg m^{-3}	3.58 ± 3.65	3.74 ± 1.53	0.08 ± 0.08	0.28 ± 0.09	0.20 ± 0.10
HNO_3, μg m^{-3}	6.65 ± 7.03	4.45 ± 3.59	0.36 ± 0.14	1.35 ± 0.66	0.50 ± 0.26
ε(NO_3^-)	39 ± 16 %	51 ± 18 %	22 ± 16 %	18 ± 6 %	26 ± 15 %
Total NO_3^-, μg m^{-3}	10.22 ± 9.74	8.19 ± 3.89	0.45 ± 0.26	1.63 ± 0.70	0.70 ± 0.28
NH_4^+, μg m^{-3}	2.06 ± 1.67	1.79 ± 0.65	0.46 ± 0.34	1.06 ± 0.25	0.40 ± 0.20
NH_3, μg m^{-3}	1.37 ± 0.90	0.75 ± 0.61	0.39 ± 0.25	0.12 ± 0.19	5.79 ± 3.67
ε(NH_4^+)	55 ± 25%	71 ± 19%	50 ± 25%	92 ± 11%	7 ± 5 %
Total NH_4^+, μg m^{-3}	3.44 ± 1.81	2.54 ± 0.89	0.78 ± 0.50	1.17 ± 0.81	6.19 ± 3.68
Na^+, μg m^{-3}	\	0.77 ± 0.39	0.03 ± 0.07	\	\
Cl^-, μgm^{-3}	\	0.64 ± 0.48	0.02 ± 0.03	\	0.01 ± 0.01
RH, %	79 ± 17	87 ± 9	74 ± 16	72 ± 9	69 ± 18
T, °C	18 ± 4	18 ± 3	25 ± 3	22 ± 3	24 ± 4
W_i, μg m^{-3}	13.9 ± 18.1	29.8 ± 20.7	5.1 ± 3.8	3.2 ± 2.8	1.6 ± 1.7
pH	1.9 ± 0.5	2.7 ± 0.3	0.9 ± 0.6	1.1 ± 0.4	2.2 ± 0.6
Reference	(Guo et al., 2017a)		(Guo et al., 2015)	(Xu et al., 2016)	This study

[a]Only during the last week of CalNex.

[b]$PM_{2.5}$ was sampled in the first half and PM_1 sampled in the second half of the study. Various parameters were similar in both cases. Crustal components were higher, but are overall generally in low concentrations so the differences had minor effects. For example, $PM_{2.5}$ Na^+ was 0.06 ± 0.09 μg m^{-3} and PM_1 Na^+ was 0.01 ± 0.01 μg m^{-3}.

Characterization of Aerosol Composition, Aerosol Acidity and Organic Acid Partitioning at an Agriculture-Intensive Rural Southeastern U.S. Site

Theodora Nah,[1,a] Hongyu Guo,[1] Amy P. Sullivan,[2] Yunle Chen,[1] David J. Tanner,[1] Athanasios Nenes,[1,3,4,5] Armistead Russell,[6] Nga Lee Ng,[1,3] L. Gregory Huey[1] and Rodney J. Weber[1,*]

[1]*School of Earth and Atmospheric Sciences, Georgia Institute of Technology, Atlanta, GA, USA*
[2]*Department of Atmospheric Science, Colorado State University, Fort Collins, CO, USA*
[3]*School of Chemical and Biomolecular Engineering, Georgia Institute of Technology, Atlanta, GA, USA*
[4]*ICE-HT, Foundation for Research and Technology, Hellas, 26504 Patras, Greece*
[5]*IERSD, National Observatory of Athens, P. Penteli, 15236, Athens, Greece*
[6]*School of Civil and Environmental Engineering, Georgia Institute of Technology, Atlanta, GA, USA*
[a]*Now at School of Energy and Environment, City University of Hong Kong, Kowloon, Hong Kong, China*

Figure S1: Map of the Yorkville field site (marked by the red diamond) and its surrounding areas (from Google Maps). Locations of nearby cattle-grazing pastures (north-west direction) and poultry CAFOs (south-east direction) are marked by the blue and white circles, respectively.

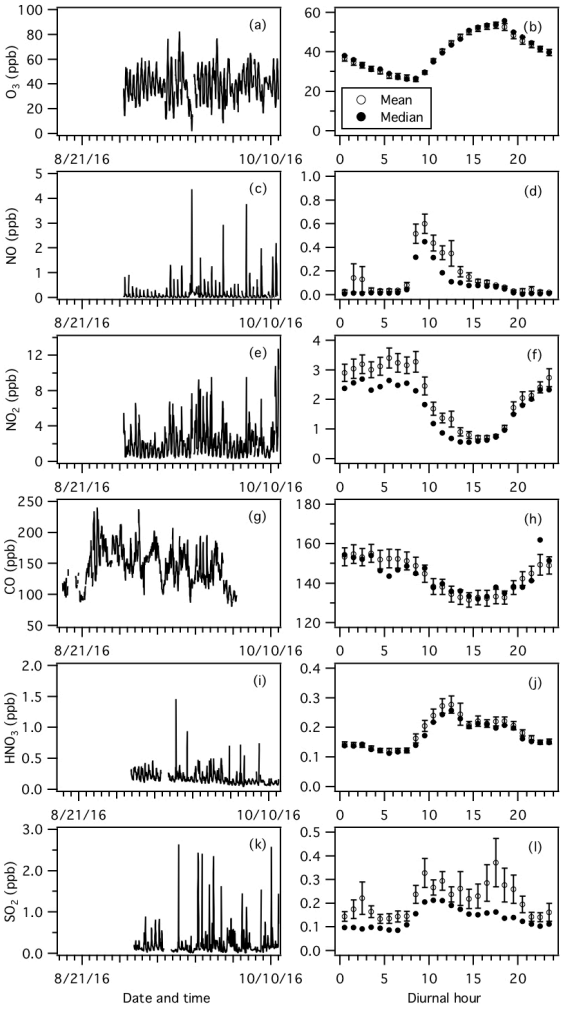

Figure S2: Time series and diurnal profiles of (a and b) O_3, (c and d) NO, (e and f) NO_2, (g and h) CO, (i and j) HNO_3, and (k and l) SO_2. Dates and times displayed are local time. All the concentrations represent averages in 1-hour intervals and the standard errors are plotted as error bars. O_3, NO, NO_2 and CO measurements were provided by the SEARCH network. HNO_3 and SO_2 were measured by the SF_6-CIMS.

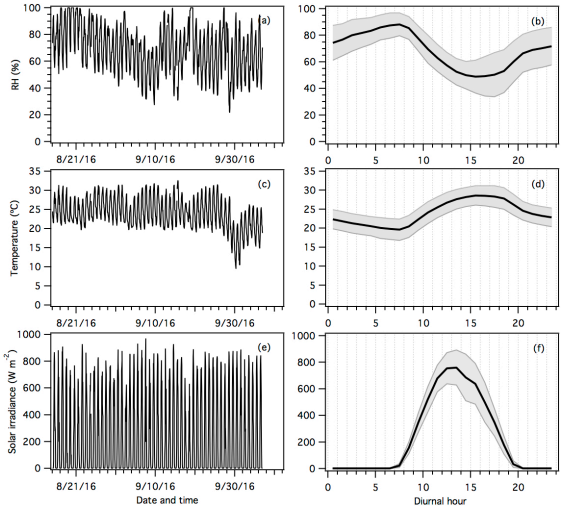

Figure S3: Time series and diurnal profiles of (a and b) RH, (c and d) temperature, and (e and f) solar irradiance. Dates and times displayed are local time. In panels b, d and f, the lines within the shaded area represents the average values. The upper and lower boundaries of the shaded areas mark one standard deviation. RH, temperature and solar irradiance measurements were provided by the SEARCH network.

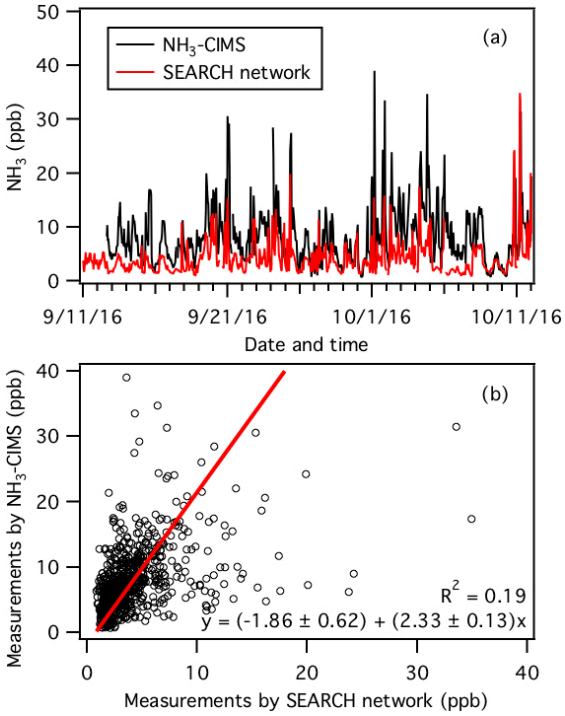

Figure S4: (a) Time series of NH_3 concentrations measured by the NH_3-CIMS and denuder-based instrument operated by the SEARCH network. (b) Comparison of NH_3 concentrations measured by the NH_3-CIMS and denuder-based instrument. The red line is the orthogonal distance regression fit to the data. All the data are displayed as 1-hour averages.

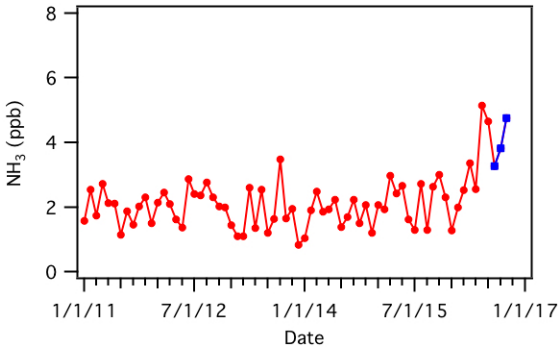

Figure S5: Monthly-averaged NH_3 concentrations at the Yorkville SEARCH monitoring site for 2011 to 2016. These measurements were made using the denuder-based instrument operated by the SEARCH network. Concentrations measured during this study (mid-August to mid-October 2016) are shown in blue.

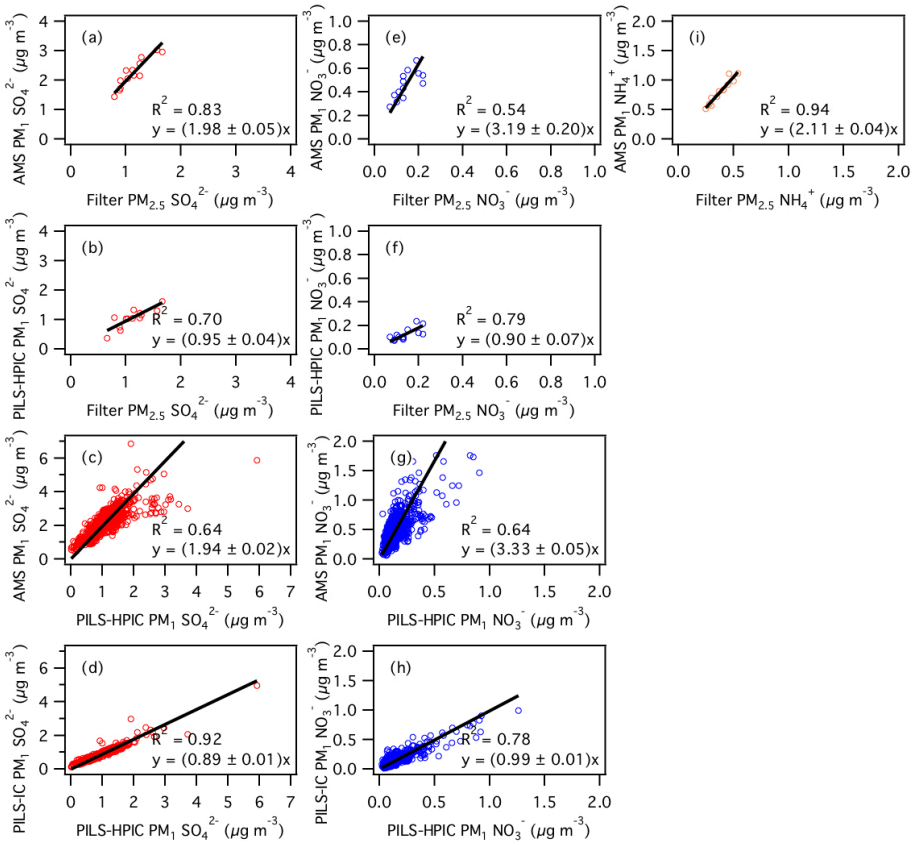

Figure S6: Aerosol (panels a to d) SO_4^{2-}, (panels e to h) NO_3^-, and (i) NH_4^+ comparisons between HR-ToF-AMS, PILS-IC, PILS-HPIC and filters for the entire field study. CDCE values were applied to the raw HR-ToF-AMS data to obtain the mass concentrations shown here (see main text for details). For comparisons between the HR-ToF-AMS, PILS-IC and PILS-HPIC data (panels c, d, g and h), the measurements are averaged over 1 hour intervals. For comparisons with filter data (panels a, b, e, f and i), the HR-ToF-AMS, PILS-IC and PILS-HPIC data are averaged over 24 hour intervals. Orthogonal regression fits are shown. Uncertainties in the fits are 1 standard deviation.

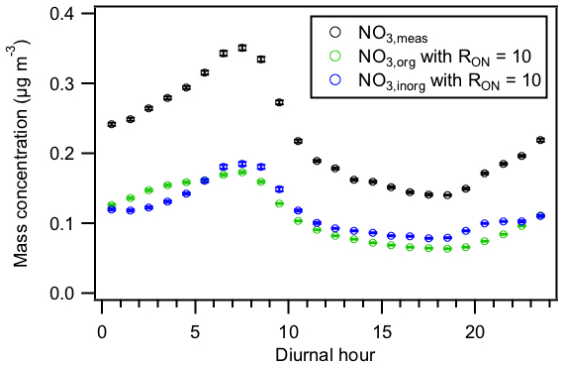

Figure S7: Diurnal profiles of the total nitrate functionality contributed by organic and inorganic nitrates ($NO_{3,meas}$), and the nitrate functionality solely from organic nitrates ($NO_{3,org}$) and inorganic nitrates ($NO_{3,inorg}$). $NO_{3,org}$ and $NO_{3,inorg}$ are estimated using the NO^+/NO_2^+ ratio method as described by Farmer et al. (2010) and Xu et al. (2015). Similar to Xu et al. (2015), we used a R_{ON} (defined here as the NO^+/NO_2^+ ratio for organic nitrates) value of 10 to calculate $NO_{3,org}$ and $NO_{3,inorg}$. All the data shown here represent averages in 1-hour intervals. Error bars shown are the standard errors.

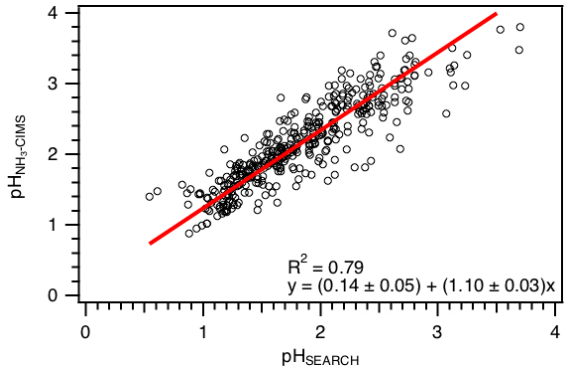

71

72 **Figure S8:** Comparison of predicted PM_1 pH values determined using NH_3-CIMS and SEARCH
73 network's NH_3 measurements as ISORROPIA-II model inputs. The other model inputs are the
74 same. The linear fit is obtained by orthogonal distance regression.

75

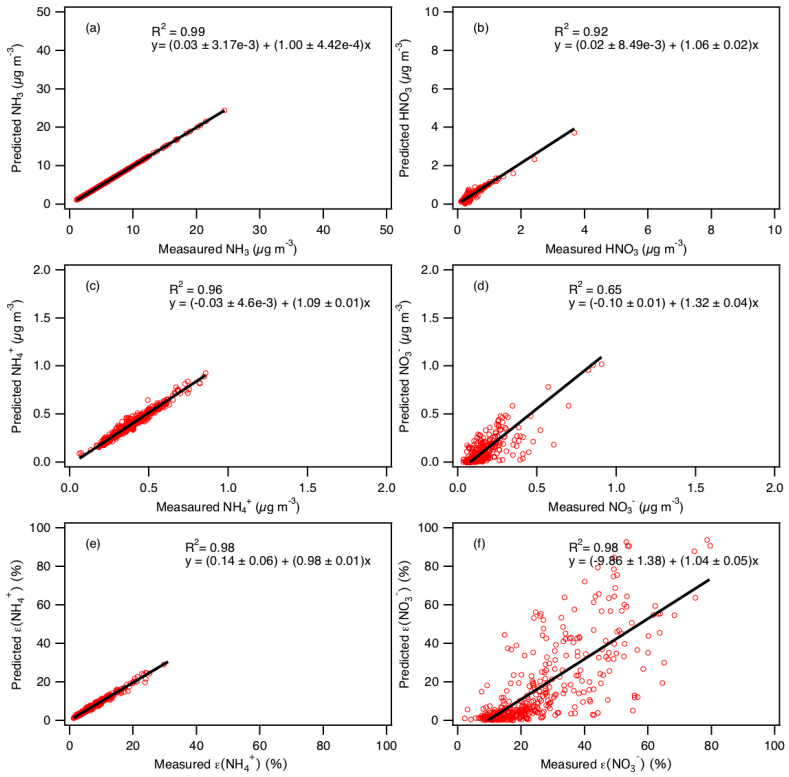

Figure S9: Comparisons of predicted and measured (a) NH_3, (b) HNO_3, (c) NH_4^+, (d) NO_3^-, (e) $\varepsilon(NH_4^+)$, and (f) $\varepsilon(NO_3^-)$. Orthogonal regression fits are shown. Uncertainties in the fits are 1 standard deviation.

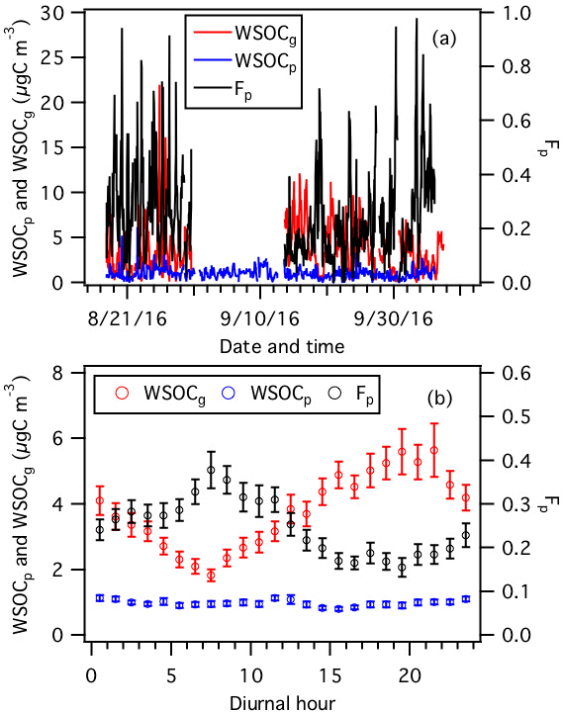

Figure S10: (a) Time series and (b) diurnal profiles of $WSOC_g$, $WSOC_p$ and F_p. Dates and times displayed are local time. All the data shown here represent averages in 1-hour intervals. Error bars shown in panel (b) are the standard errors. $F_p = WSOC_p / (WSOC_p + WSOC_g)$.

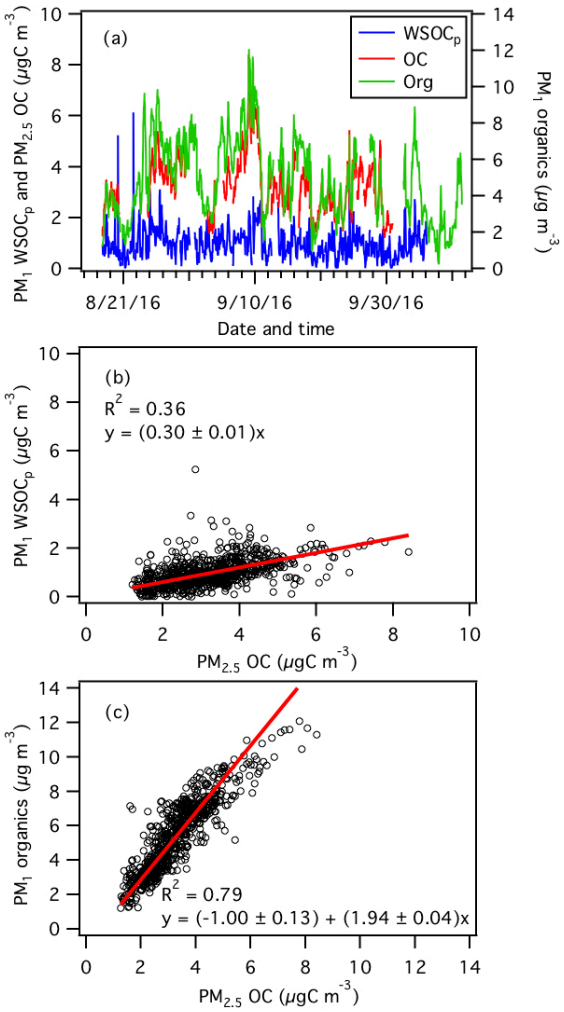

Figure S11: (a) Time series of HR-ToF-AMS organics, $WSOC_p$ and OC. (b) Linear regression correlation between $WSOC_p$ and OC. (c) Linear regression correlation between HR-ToF-AMS organics and OC. All the data shown here represent averages in 1-hour intervals. Note that OC measurements are $PM_{2.5}$, while $WSOC_p$ and HR-ToF-AMS organics measurements are PM_1. Linear fits are obtained by orthogonal distance regression.

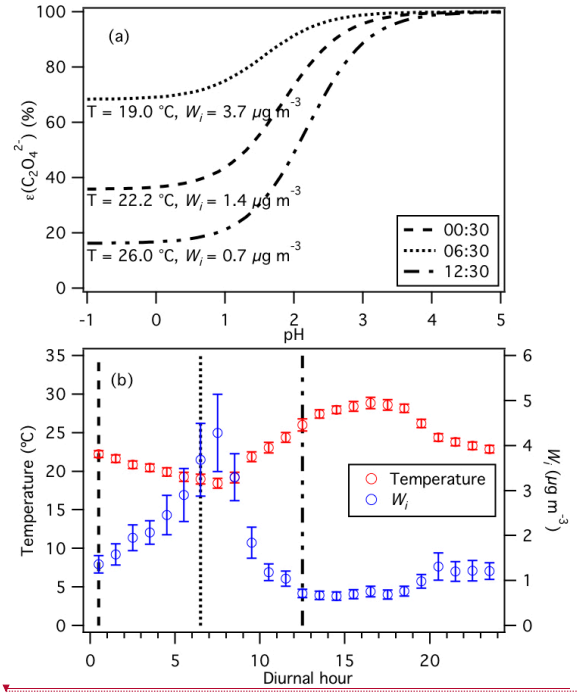

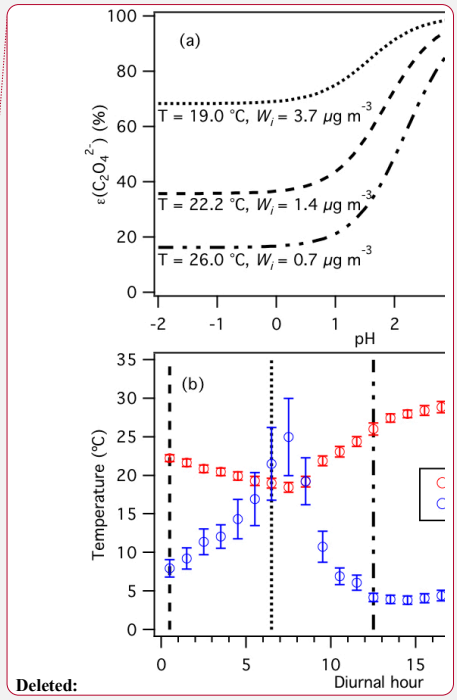

Deleted:

Figure S12: (a) Analytically calculated S curves of $\varepsilon(C_2O_4^{2-})$ at different times of the day: 00:30, 06:30 and 12:30. These S curves are calculated using values obtained from (b) the diurnal profiles of temperature and W_i. The set of 1-hour average temperatures and W_i at diurnal hours 00:30, 06:30 and 12:30 is used to calculate each S curve shown in panel (a). Similar to Fig. 7, we used $\gamma_{C_2H_2O_4}$ = 0.0492 (AIOMFAC predicted) and assumed that $\gamma_{H^+-NO_3^-} = \sqrt{\gamma_{H^+}\gamma_{NO_3^-}} = \sqrt{\gamma_{H^+}\gamma_{C_2HO_4^-}}$ = 0.265 (ISORROPIA-II predicted) to generate these S curves.

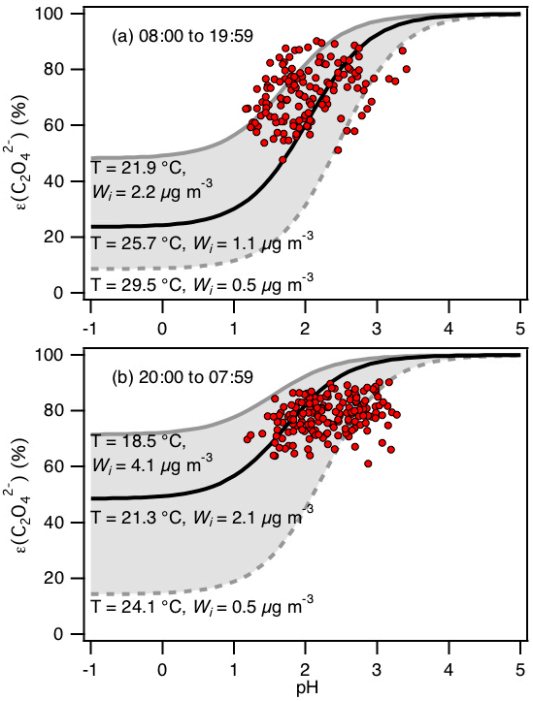

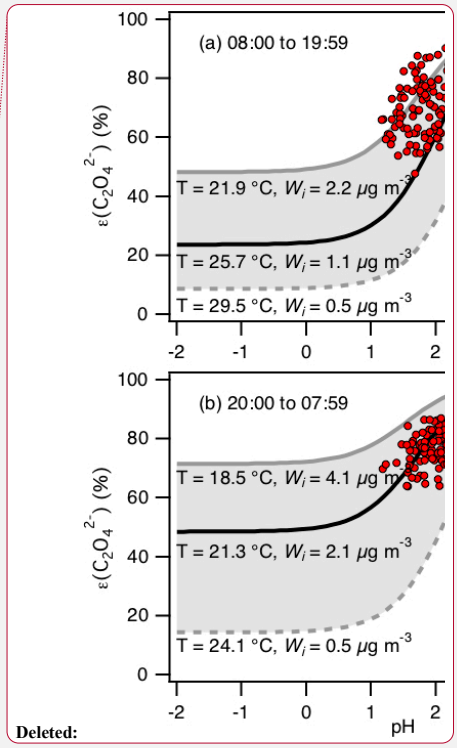

Deleted:

Figure S13: Analytically calculated S curve of ε($C_2O_4^{2-}$) and ambient data from 13 September to 6 October 2016 plotted against ISORROPIA-predicted particle pH. For the ambient data, a narrow range in W_i (0.5 to 4 μg m^{-3}) and RH (20 to 90 %) is chosen to be close to the analytically calculated outputs. We divided the ambient data into two sets: panel (a) 08:00 to 19:59, and panel (b) 20:00 to 07:59. For both analytically calculated S curves, we used $\gamma_{C_2H_2O_4}$ = 0.0492 (AIOMFAC predicted). We also assumed that $\gamma_{H^+}\gamma_{C_2HO_4^-} = \gamma_{H^+}\gamma_{NO_3^-}$, and used the ISORROPIA-predicted $\gamma_{H^+-NO_3^-} = \sqrt{\gamma_{H^+}\gamma_{NO_3^-}}$ = 0.265. In panel (a), we used the average temperature and W_i (25.7 ± 3.8 °C and 1.1 ± 1.1 μg m^{-3}) for the data between 08:00 to 19:59 to calculate the S curve (black line). In panel (b), we used the average temperature and W_i (21.3 ± 2.8 °C and 2.1 ± 2.0 μg m^{-3}) for the data between 20:00 to 07:59 to calculate the S curve (black line). Grey lines in both panels are S curves calculated using one standard deviation from the average temperature and W_i for the two datasets. In panel (a), the dotted grey line is the S curve calculated using 29.5 °C and 0.5 μg m^{-3}

while the solid grey line is the S curve calculated using 21.9 °C and 2.2 μg m^{-3}. In panel (b), the dotted grey line is the S curve calculated using 24.1 °C and 0.5 μg m^{-3} while the solid grey line is the S curve calculated using 18.5 °C and 4.1 μg m^{-3}.

Table S1: List of gas-phase acids measured by SF_6-CIMS, and their measurement uncertainties and detection limits.

Acid	Measurement uncertainty (%)	Detection limits (ppb)[a]
Nitric acid	13	0.20
Formic acid	12	0.03
Acetic acid	12	0.06
Oxalic acid	14	1×10^{-3}
Butyric acid	14	0.03
Glycolic acid	22	2×10^{-3}
Propionic acid	14	6×10^{-3}
Valeric acid	22	0.01
Malonic acid	25	7×10^{-4}
Succinic acid	25	3×10^{-3}

[a]Detection limits are approximated from 3 times the standard deviation values (3σ) of the ion signals measured during background mode. Shown here are the average detection limits of the organic acids for 2.5 min integration periods which corresponds to the length of a background measurement at a 0.04 s duty cycle for each mass.

S1. SF_6-CIMS calibration of gas-phase HNO_3 and organic acids

Detailed descriptions of post-field laboratory calibrations of HNO_3, oxalic, butyric, glycolic, propionic, valeric, malonic and succinic acids can be found in Nah et al. (2018). The response of the CIMS acid signals were measured relative to the sensitivity of $^{34}SO_2$ in these calibration measurements.

The HNO_3 calibration source was a permeation tube (KIN-TEK) whose emission rate was measured using UV optical absorption (Neuman et al., 2003). Solid or liquid samples of oxalic (Sigma Aldrich, ≥ 99 %), butyric (Sigma Aldrich, ≥ 99 %), glycolic (Sigma Aldrich, 99 %), propionic (Sigma Aldrich, ≥ 99.5 %), valeric (Sigma Aldrich, ≥ 99 %), malonic (Sigma Aldrich, ≥ 99.5 %) and succinic (Sigma Aldrich, 99 %) acids were used in calibration measurements. The acid sample was placed in a glass impinger, which was immersed in a water bath at a fixed temperature to provide a constant vapor pressure. For oxalic, butyric, glycolic, propionic and valeric acids, the water bath temperature was set to 0 ˚C. For malonic and succinic acids, the water bath temperature was set to 40 ˚C in order to generate large enough gas phase concentrations for calibration. 6 to 10 mL min^{-1} of nitrogen gas (N_2) was passed over the organic acid in the glass impinger. This organic acid air stream was diluted with different N_2 flows (1 to 5 L min^{-1}) to obtain different mixing ratios of the organic acid. We calculated the mixing ratios based on the acid's emission rate from the impinger or the acid's vapor pressure. Emission rates of gas-phase oxalic, malonic and succinic acids from the impinger were measured by scrubbing the output of the impinger in deionized water, followed by ion chromatography analysis. We measured the vapor pressures of butyric and propionic acids at 0 ˚C using a capacitance manometer (MKS Instruments). We estimated the vapor pressures of glycolic and valeric acids at 0 ˚C using their literature vapor pressures at 25 ˚C and enthalpies of vaporization (Daubert and Danner, 1989; Lide, 1995; Acree and Chickos, 2010).

S2. $WSOC_p$ and OC

We estimated the water-soluble fraction of OC by comparing the $WSOC_p$ and OC measurements. The time series of organics, $WSOC_p$ and OC are shown in Fig. S11a. As shown in Fig. S11b, $WSOC_p$ is moderately correlated with OC at the site. The orthogonal distance regression fit suggests that 30 % of the OC is water-soluble (estimated measurement uncertainty of 19 %),

which is significantly smaller than the fraction (61 %) measured during the SOAS study (Xu et al., 2017). This difference may be due, in part, to the $WSOC_p$/OC ratio for this study being under-estimated. $WSOC_p$ are PM_1 measurements while OC are $PM_{2.5}$ measurements. This is in contrast to the SOAS study where both $WSOC_p$ and OC are $PM_{2.5}$ measurements. PM_1 organics mass concentration is highly correlated with OC and has an orthogonal distance regression slope of 1.94 (Fig. S9c), which is similar to the value (1.92) reported for the SOAS study (Xu et al., 2017).

S3. $C_2H_2O_4$- $C_2O_4^{2-}$ partitioning

Here, we show the detailed derivation of equation (4) in that paper. Equilibrium between gaseous $C_2H_2O_4$ and particle-phase $C_2O_4^{2-}$ involves the dissolution of $C_2H_2O_4$ into the aqueous phase (assuming particles are liquids), followed by dissociation of the dissolved $C_2H_2O_4$:

$$C_2H_2O_4(\mathrm{g}) \leftrightarrow C_2H_2O_4(\mathrm{aq}) \quad H_{C_2H_2O_4}$$

$$C_2H_2O_4(\mathrm{aq}) \leftrightarrow C_2HO_4^-(\mathrm{aq}) + H^+(\mathrm{aq}) \quad K_{a1}$$

$$C_2HO_4^-(\mathrm{aq}) \leftrightarrow C_2O_4^{2-}(\mathrm{aq}) + H^+(\mathrm{aq}) \quad K_{a2}$$

for which the reaction equilibriums are expressed as follows:

$$H_{C_2H_2O_4} = \gamma_{C_2H_2O_4}[C_2H_2O_4]/p_{C_2H_2O_4} \quad (1)$$

$$K_{a1} = \frac{\gamma_{H^+}[H^+]\gamma_{C_2HO_4^-}[C_2HO_4^-]}{\gamma_{C_2H_2O_4}[C_2H_2O_4]} \quad (2)$$

$$K_{a2} = \frac{\gamma_{H^+}[H^+]\gamma_{C_2O_4^{2-}}[C_2O_4^{2-}]}{\gamma_{C_2HO_4^-}[C_2HO_4^-]} \quad (3)$$

where $H_{C_2H_2O_4}$ (mole L^{-1} atm^{-1}) is the Henry's law constant for oxalic acid, K_{a1} and K_{a2} (mole L^{-1}) are the first and second acid dissociation constants for oxalic acid, $p_{C_2H_2O_4}$ (atm) is the partial pressure of oxalic acid in the atmosphere, and γ_i's are activity coefficients. In equations (1) to (3), [x] represents aqueous concentrations (mole L^{-1}).

The total dissolved $C_2H_2O_4$ or particle-phase oxalate ($C_2O_4^{\mathrm{T}}$) can be expressed as:

$$[C_2HO_4^{\mathrm{T}}] = [C_2H_2O_4] + [C_2HO_4^-] + [C_2O_4^{2-}] \quad (4)$$

Using equations (1) to (3), $[C_2O_4^{\mathrm{T}}]$ can be expressed as:

$$[C_2O_4^{\mathrm{T}}] = H_{C_2H_2O_4} p_{C_2H_2O_4} \left(\frac{1}{\gamma_{C_2H_2O_4}} + \frac{K_{a1}}{\gamma_{H^+}\gamma_{C_2HO_4^-}[H^+]} + \frac{K_{a1}K_{a2}}{\gamma_{H^+}\gamma_{H^+}\gamma_{C_2O_4^{2-}}[H^+]^2} \right) \quad (5)$$

The ideal gas law gives:

$$c(C_2H_2O_4) = \frac{p_{C_2H_2O_4}}{RT} \quad (6)$$

where R is the gas constant, T is temperature, and c(x) represents concentration per volume of air (mole m^{-3}). The particle-phase fraction of oxalate can then be expressed as:

$$\varepsilon(C_2O_4^{2-}) = \frac{c(C_2O_4^{\mathrm{T}})}{c(C_2H_2O_4)+c(C_2O_4^{\mathrm{T}})} = \frac{[C_2HO_4^{\mathrm{T}}]W_i}{c(C_2H_2O_4)+[C_2HO_4^{\mathrm{T}}]W_i} \quad (7)$$

where W_i is the particle liquid water content associated with inorganic species (μg m^{-3}; mass per volume of air). Note that the particle liquid water content associated with organic species is not considered in this case, but it can be included. Alternatively, the measured particle water can be used.

By putting equations (5) and (6) into equation (7), $\varepsilon(C_2O_4^{2-})$ can be expressed as:

$$\varepsilon(C_2O_4^{2-}) = \frac{H_{C_2H_2O_4} W_i RT \left(\frac{1}{\gamma_{C_2H_2O_4}} + \frac{K_{a1}}{\gamma_{H^+}\gamma_{C_2HO_4^-}[H^+]} + \frac{K_{a1}K_{a2}}{\gamma_{H^+}\gamma_{H^+}\gamma_{C_2O_4^{2-}}[H^+]^2} \right)}{1 + H_{C_2H_2O_4} W_i RT \left(\frac{1}{\gamma_{C_2H_2O_4}} + \frac{K_{a1}}{\gamma_{H^+}\gamma_{C_2HO_4^-}[H^+]} + \frac{K_{a1}K_{a2}}{\gamma_{H^+}\gamma_{H^+}\gamma_{C_2O_4^{2-}}[H^+]^2} \right)} \quad (8)$$

At 298 K, K_{a1} = 5.62 x 10^{-2} mole L^{-1} and K_{a2} = 1.55 x 10^{-4} mole L^{-1} (Haynes, 2014). Assuming that $\gamma_{H^+} = 1$, $K_{a1}K_{a2} \ll \gamma_{H^+}\gamma_{H^+}\gamma_{C_2O_4^{2-}}[H^+]^2$ for the conditions of our study. Hence, equation (8) can be simplified to:

$$\varepsilon(C_2O_4^{2-}) \cong \frac{H_{C_2H_2O_4} W_i RT \left(\frac{\gamma_{H^+}\gamma_{C_2HO_4^-}}{\gamma_{C_2H_2O_4}}[H^+] + K_{a1} \right)}{\gamma_{H^+}\gamma_{C_2HO_4^-}[H^+] + H_{C_2H_2O_4} W_i RT \left(\frac{\gamma_{H^+}\gamma_{C_2HO_4^-}}{\gamma_{C_2H_2O_4}}[H^+] + K_{a1} \right)} \quad (9)$$

After accounting for the SI units and substituting $[H^+] = 10^{-pH}$, equation (9) becomes:

$$\varepsilon(C_2O_4^{2-}) \cong \frac{H_{C_2H_2O_4} W_i RT\left(\frac{\gamma_H+\gamma_{C_2HO_4^-}}{\gamma_{C_2H_2O_4}}10^{-pH}+K_{a1}\right)\times 0.987\times 10^{-14}}{\gamma_{H^+}\gamma_{C_2HO_4^-}10^{-pH}+H_{C_2H_2O_4} W_i RT\left(\frac{\gamma_H+\gamma_{C_2HO_4^-}}{\gamma_{C_2H_2O_4}}10^{-pH}+K_{a1}\right)\times 0.987\times 10^{-14}} \quad (10)$$

Note that 0.987 x 10^{-14} comes from using R = 8.314 m^3 Pa K^{-1} mol^{-1}, and hence needing to convert 1 atm to 1 Pa and 1 L to 1 µg. We used the average of $H_{C_2H_2O_4}$ values provided by Clegg et al. (1996), Compernolle and Muller (2014) and Saxena and Hildemann (1996) (6.11 x 10^8 mole L^{-1} atm^{-1} at 25 °C), and accounted for the effect of temperature using equation 19 in Sander (2015). Although K_{a1} also depends on temperature, the K_{a1} value at 25 °C (5.62 x 10^{-2}, (Haynes, 2014)) is used for all the oxalic acid S curve calculations in this paper since equations that determine temperature-dependent K_{a1} values are not available. In addition, the temperatures observed in this study are close to 25 °C.

Figure S12 provides a conceptual picture of how the relationship between $\varepsilon(C_2O_4^{2-})$ and particle pH can change based on the time of the day. Different S curves for $\varepsilon(C_2O_4^{2-})$ are calculated using equation (10) and 1-hour average values obtained from the diurnal profiles of temperature and W_i (specifically at 00:30, 06:30 and 12:30). The S curves are shown to differ substantially due to the diurnal variations of temperature and W_i. For example, a decrease in temperature and an increase in W_i from 00:30 to 06:30 will result in the S curve shifting to the left, which indicates that a substantially higher fraction of gas-phase oxalic acid will partition to the particle phase for a given particle pH at 06:30 compared to at 00:30. Higher W_i also increases the fraction of oxalate that partitions to the particle phase due solely to solubility, as seen from the plateau regions at low pH in Fig. S12. Conversely, an increase in temperature and a decrease in W_i from 06:30 to 12:30 will result in a considerably lower fraction of gas-phase oxalic acid partitioning to the particle phase for a given particle pH at 12:30 compared to at 06:30.

S4. PILS-HPIC denuder efficiency

Post-field laboratory experiments were performed to determine if disagreements between the measured and predicted molar fractions of formic and acetic acid in the particle phase were due to positive biases in particle-phase PILS-HPIC measurements as a result of less than 100 % gas removal denuder efficiency and uptake of gases in the PILS liquid system. While experiments were done solely with formic acid, similar results are expected for acetic acid. In these

experiments, liquid formic acid (Sigma Aldrich, ≥ 99 %) was diluted with ultrapure deionized water and placed in a bubbler. A flow of 18 mL min^{-1} of N_2 was passed through the formic acid in the bubbler. This formic acid air stream was then passed through a nafion dryer and diluted with 52 L min^{-1} of N_2. Two experiments were performed. In the first experiment, the diluted formic acid air flow was introduced directly into the PILS, which was connected to a Metrohm 761 Compact IC (Metrohm AG). In the second experiment, the diluted formic acid air flow was passed through a 28 cm parallel plate carbon denuder (Sunset Lab) prior to introduction into the PILS-IC system.

Our experiments showed that the IC detected formate when the diluted formic acid air flow was introduced directly into the PILS-IC system. IC analysis revealed that the gas-phase formic acid concentration was ~75 μg m^{-3}. However, no formate was detected above the limit of detection (0.02 μg m^{-3}) when the diluted formic acid air flow was passed through the carbon denuder prior to introduction into the PILS-IC system. These measurements indicated that the carbon denuder has a ≥ 99.97 % formic acid gas removal efficiency. Hence, these experiments indicate that the carbon denuder removes the formic acid gas completely. We conclude that disagreements between the measured and predicted molar fractions of formic and acetic acid in the particle phase were not due to positive biases in particle-phase formate and acetate PILS-HPIC measurements as a result of less than 100 % gas removal denuder efficiency.

S5. Particle-phase formic and acetic acid dimers

Previous studies have shown that formic and acetic acid dimers may form in the aqueous phase (Schrier et al., 1964; Gilson et al., 1997; Chen et al., 2008). If the aforementioned acid dimers are present in aerosols, equilibrium between gas-phase formic/acetic acid (denoted as HA) and particle-phase formate/acetate (denoted as A^-) will differ from that predicted assuming no dimers existed, as done in the main text.

The dissolution of HA into the aqueous phase (assuming particles are liquids), followed by the formation of particle-phase dimers (denoted as $((HA)_2)$ and dissociation of the dissolved HA:

$$HA\ (g) \leftrightarrow HA\ (aq) \quad H_{HA}$$

$$HA\ (aq) \leftrightarrow (HA)_2\ (aq) \quad K_{dim}$$

$$HA\ (\mathrm{aq}) \leftrightarrow\ A^-\ (\mathrm{aq}) +\ H^+(\mathrm{aq}) \quad K_{a1}$$

for which the reaction equilibriums are expressed as follows:

$$H_{HA} = \gamma_{HA}[HA]/p_{HA} \tag{11}$$

$$K_{dim} = \frac{[(HA)_2]}{[HA]^2} \tag{12}$$

$$K_{a1} = \frac{\gamma_{A^-}[A^-]\gamma_{H^+}[H^+]}{\gamma_{HA}[HA]} \tag{13}$$

where H_{HA} (mole L^{-1} atm^{-1}) is the Henry's law constant for formic or acetic acid, K_{a1} (mole L^{-1}) is the first acid dissociation constants for formic or acetic acid, p_{HA} (atm) is the partial pressure of formic or acetic acid in the atmosphere, K_{dim} (L $mole^{-1}$) is the dimerization constant, and γ_i's are activity coefficients. In equations (11) to (13), [x] represents aqueous concentrations (mole L^{-1}).

The total dissolved formate or acetate (A^T) can be expressed as:

$$[A^T] = [HA] + [A^-] +\ [(HA)_2] \tag{14}$$

Using equations (11) to (13), $[A^T]$ can be expressed as:

$$[A^T] = H_{HA}p_{HA}\left(\frac{1}{\gamma_{HA}} + \frac{K_{a1}}{\gamma_{H^+}\gamma_{A^-}[H^+]} + \frac{K_{dim}H_{HA}p_{HA}}{\gamma_{HA}\gamma_{HA}}\right) \tag{15}$$

The ideal gas law gives:

$$c(HA) = \frac{p_{HA}}{RT} \tag{16}$$

where R is the gas constant, T is temperature, and c(x) represents concentration per volume of air (mole m^{-3}). The particle-phase fraction of formate or acetate can then be expressed as:

$$\varepsilon(A^-) = \frac{c(A^T)}{c(HA)+c(A^T)} = \frac{[A^T]W_i}{c(HA)+[A^T]W_i} \tag{17}$$

where W_i is the particle liquid water content associated with inorganic species (μg m^{-3}; mass per volume of air). Particle liquid water content associated with organic species is not considered in this case, but it can be included. Alternatively, the measured particle water can be used.

By putting equations (15) and (16) into equation (17), and accounting for the SI units, $\varepsilon(A^-)$ can ultimately be expressed as:

$$\varepsilon(A^-) = \frac{H_{H_{HA}} W_i RT\left(\frac{1}{\gamma_{HA}} + \frac{K_{a1}}{\gamma_{H^+}\gamma_{A^-}10^{-pH}} + \frac{K_{dim} H_{HA} p_{HA}}{\gamma_{HA}\gamma_{HA}}\right)\times 0.987\times 10^{-14}}{1 + H_{H_{HA}} W_i RT\left(\frac{1}{\gamma_{HA}} + \frac{K_{a1}}{\gamma_{H^+}\gamma_{A^-}10^{-pH}} + \frac{K_{dim} H_{HA} p_{HA}}{\gamma_{HA}\gamma_{HA}}\right)\times 0.987\times 10^{-14}} \quad (18)$$

At 298 K, K_{a1} values are 1.78 x 10^{-4} mole L^{-1} and 1.75 x 10^{-5} mole L^{-1} for formic and acetic acid, respectively (Haynes, 2014). K_{dim} values are 0.56 L $mole^{-1}$ and 0.92 L $mole^{-1}$ for formic and acetic acid, respectively (Chen et al., 2008). Temperature-dependent H_{HA} values for formic and acetic acid can be obtained from Sander (2015). p_{HA} can be calculated from the measured gas-phase formic or acetic acid concentrations (μg m^{-3}) and the ideal gas law. We used the web version of AIOMFAC (www.aiomfac.caltech.edu) (Zuend et al., 2008; Zuend et al., 2011; Zuend et al., 2012) to compute study-averaged γ_{HA} values of 0.334 and 2.150 for formic and acetic acid, respectively. We assumed that $\gamma_{H^+}\gamma_{A^-} = \gamma_{H^+}\gamma_{NO_3^-} = 0.07$ for both formic and acetic acid.

Comparison of S curves generated from equation (18) and those generated from equations (5) and (6) in the main text (which assumed that no dimers existed) showed that accounting for the presence of acid dimers increased predicted $\varepsilon(A^-)$ values by less than 1 % for particle pH 0.9 to 3.8 (i.e., pH values in this study). S curves generated by equation (18) also do not match our measured molar fractions of formic and acetic acid in the particle phase. This analysis shows that the molar fractions of formic and acetic acid in the particle phase do not change substantially when the presence of particle-phase acid dimers is accounted for due to the somewhat low H_{HA} values for formic and acetic acid. Hence, disagreements between the measured and predicted molar fractions of formic and acetic acid in the particle phase are not due to the presence of particle-phase formic and acetic acid dimers.

References

Acree, W., and Chickos, J. S.: Phase Transition Enthalpy Measurements of Organic and Organometallic Compounds. Sublimation, Vaporization and Fusion Enthalpies From 1880 to 2010, J. Phys. Chem. Ref. Data, 39, 942, 10.1063/1.3309507, 2010.

Chen, J. H., Brooks, C. L., and Scheraga, H. A.: Revisiting the carboxylic acid dimers in aqueous solution: Interplay of hydrogen bonding, hydrophobic interactions, and entropy, Journal of Physical Chemistry B, 112, 242-249, 10.1021/jp074355h, 2008.

Clegg, S. L., Brimblecombe, P., and Khan, L.: The Henry's law constant of oxalic acid and its partitioning into the atmospheric aerosol, Idojaras, 100, 51-68, 1996.

Compernolle, S., and Muller, J. F.: Henry's law constants of diacids and hydroxy polyacids: recommended values, Atmos. Chem. Phys., 14, 2699-2712, 10.5194/acp-14-2699-2014, 2014.

Daubert, T. E., and Danner, R. P.: Physical and thermodynamic properties of pure chemicals: data compilation, Taylor & Francis, Washington, DC, 1989.

Farmer, D. K., Matsunaga, A., Docherty, K. S., Surratt, J. D., Seinfeld, J. H., Ziemann, P. J., and Jimenez, J. L.: Response of an aerosol mass spectrometer to organonitrates and organosulfates and implications for atmospheric chemistry, Proceedings of the National Academy of Sciences of the United States of America, 107, 6670-6675, 10.1073/pnas.0912340107, 2010.

Gilson, M. K., Given, J. A., Bush, B. L., and McCammon, J. A.: The statistical-thermodynamic basis for computation of binding affinities: A critical review, Biophysical Journal, 72, 1047-1069, 10.1016/s0006-3495(97)78756-3, 1997.

Haynes, W. M.: CRC handbook of chemistry and physics: A ready-reference book of chemical and physical data. , Boca Raton: CRC Press, 2014.

Lide, D. R.: CRC handbook of chemistry and physics: a ready-reference book of chemical and physical data, CRC Press, Boca Raton, FL, 1995.

Nah, T., Ji, Y., Tanner, D. J., Guo, H., Sullivan, A. P., Ng, N. L., Weber, R. J., and Huey, L. G.: Real-time measurements of gas-phase organic acids using SF6- chemical ionization mass spectrometry, Atmos. Meas. Tech. Discuss., 2018, 1-40, 10.5194/amt-2018-46, 2018.

Neuman, J. A., Ryerson, T. B., Huey, L. G., Jakoubek, R., Nowak, J. B., Simons, C., and Fehsenfeld, F. C.: Calibration and evaluation of nitric acid and ammonia permeation tubes by UV optical absorption, Environmental Science & Technology, 37, 2975-2981, 10.1021/es0264221, 2003.

Sander, R.: Compilation of Henry's law constants (version 4.0) for water as solvent, Atmos. Chem. Phys., 15, 4399-4981, 10.5194/acp-15-4399-2015, 2015.

Saxena, P., and Hildemann, L. M.: Water-soluble organics in atmospheric particles: A critical review of the literature and application of thermodynamics to identify candidate compounds, Journal of Atmospheric Chemistry, 24, 57-109, 10.1007/bf00053823, 1996.

Schrier, E. E., Pottle, M., and Scheraga, H. A.: The Influence of Hydrogen and Hydrophobic Bonds on the Stability of the Carboxylic Acid Dimers in Aqueous Solution, Journal of the American Chemical Society, 86, 3444-3449, 10.1021/ja01071a009, 1964.

Xu, L., Suresh, S., Guo, H., Weber, R. J., and Ng, N. L.: Aerosol characterization over the southeastern United States using high-resolution aerosol mass spectrometry: spatial and seasonal variation of aerosol composition and sources with a focus on organic nitrates, Atmos. Chem. Phys., 15, 7307-7336, 10.5194/acp-15-7307-2015, 2015.

Xu, L., Guo, H. Y., Weber, R. J., and Ng, N. L.: Chemical Characterization of Water-Soluble Organic Aerosol in Contrasting Rural and Urban Environments in the Southeastern United States, Environmental Science & Technology, 51, 78-88, 10.1021/acs.est.6b05002, 2017.

Zuend, A., Marcolli, C., Luo, B. P., and Peter, T.: A thermodynamic model of mixed organic-inorganic aerosols to predict activity coefficients, Atmos. Chem. Phys., 8, 4559-4593, 10.5194/acp-8-4559-2008, 2008.

Zuend, A., Marcolli, C., Booth, A. M., Lienhard, D. M., Soonsin, V., Krieger, U. K., Topping, D. O., McFiggans, G., Peter, T., and Seinfeld, J. H.: New and extended parameterization of the

thermodynamic model AIOMFAC: calculation of activity coefficients for organic-inorganic mixtures containing carboxyl, hydroxyl, carbonyl, ether, ester, alkenyl, alkyl, and aromatic functional groups, Atmos. Chem. Phys., 11, 9155-9206, 10.5194/acp-11-9155-2011, 2011.

Zuend, A., Marcolli, C., Luo, B. P., and Peter, T.: A thermodynamic model of mixed organic-inorganic aerosols to predict activity coefficients (vol 8, pg 4559, 2008), Atmos. Chem. Phys., 12, 10075-10075, 10.5194/acp-12-10075-2012, 2012.